Review Vol. 29, No. 8 / 12 April 2021 / Optics Express 12543

Optics EXPRESS

Review of optical sensing and manipulation of chiral molecules and nanostructures with the focus on plasmonic enhancements [Invited]

ANEETH KAKKANATTU,[1,2] NARIMA EERQING,[1,2] SHAHIN GHAMARI,[1,2] AND FRANK VOLLMER[1,*]

[1] *Living Systems Institute, Physics and Astronomy, University of Exeter, EX4 4QD, UK*
[2] *These authors contributed equally*
[*] *f.vollmer@exeter.ac.uk*

Abstract: Chiral molecules are ubiquitous in nature; many important synthetic chemicals and drugs are chiral. Detecting chiral molecules and separating the enantiomers is difficult because their physiochemical properties can be very similar. Here we review the optical approaches that are emerging for detecting and manipulating chiral molecules and chiral nanostructures. Our review focuses on the methods that have used plasmonics to enhance the chiroptical response. We also review the fabrication and assembly of (dynamic) chiral plasmonic nanosystems in this context.

1. Introduction

Plasmonic nanoparticles and nanostructures with dimensions smaller than the wavelength of the incident light can manipulate light in both the near- and far-field zones and control the phase and spin angular momentum of light. Moreover, they can enhance the interactions of light with matter, such as the interaction with molecules that are placed in the vicinity of the nanoparticle's plasmon-enhanced near-field. In noble metal nanoparticles such as those made of gold, silver, and palladium, the incident light beam induces the collective oscillation of conduction band electrons which leads to resonance known as the localized surface plasmon resonance (LSPR). These electron oscillations confine electromagnetic fields to nanoscale regions, the LSPR hotspots. In LSPR hotspots, the field can be several orders of magnitude more intense as compared to the incident field exciting the resonance. LSPR hotspots are often more highly localized as compared to the fields associated with propagating surface plasmon resonances (SPR) of extended metallic films [1–6].

LSPR plays a crucial role in sensing because its localized near-field enables an exceedingly high detection sensitivity for the molecules that bind within an LSPR hotspot [7–10]. When combined with the high-quality factor resonances of an optical microcavity, i.e., a 100 µm glass microsphere, the resulting plasmon-coupled microcavity sensor (called optoplasmonic sensor) has been used for the detection of small molecules with less than one kilodalton of molecular weight, and for the detection of single atomic ions in aqueous solution [6,11–13].

In all of the LSPR-based sensing approaches discussed here, the binding of a molecule is detected from a resonance peak-shift/change that is observed in the transmission or reflection spectrum. The detection sensitivity of the LSPR and optoplasmonic sensing assays typically does not increase with the application of a higher optical power, and this is different from other LSPR-based sensing techniques such as those based on surface-enhanced Raman scattering. However, exciting LSPR-based sensors [14–16] with a high intensity beam can influence the molecular processes that take place on, or in the proximity of, the plasmonic nanoparticles and

#421839
Journal © 2021

https://doi.org/10.1364/OE.421839
Received 2 Feb 2021; revised 23 Mar 2021; accepted 23 Mar 2021; published 8 Apr 2021

their hotspots. For example, the chemical manipulation of molecules by optical excitation of LSPR has been demonstrated with the precise cleaving of Au-S thiol bonds [17]. In general, the excitation of LSPR can be used to generate hot electrons and holes, and they can participate in diverse types of redox reactions with ligand molecules [18,19].

Chiroptical spectroscopy, in the broadest sense, uses light for the specific detection and discrimination of chiral molecules. Chiral molecules have two possible three-dimensional (3D) structures that are mirror images of each other and that are known as the pair of enantiomers. The specific detection of enantiomers is particularly important because chiral molecules are found throughout nature; examples of this are amino acids, nucleotides, sugars, and their macromolecular counterparts, which are proteins, nucleic acids and carbohydrates, respectively. Furthermore, many small organic molecules are chiral and this includes drugs, antibiotics, toxins, and metabolites [20]. The organic synthesis of chiral molecules often results in a racemic (50:50) mixture of the two enantiomers. One finds pronounced differences in the pharmacology of the enantiomers for some of the chiral drugs. This is one of the reasons why it is particularly important to develop techniques capable of analyzing the exact composition of a mixture of chiral molecules and to develop techniques that can separate the enantiomers. Examples of established chiroptical techniques capable of detecting chiral molecules and discriminating their enantiomers are polarimetry, circular dichroism (CD), and optical rotatory dispersion (ORD) as well as vibrational Raman optical activity (VROA) spectroscopy. CD makes use of the difference in the absorption of circularly polarized light (CPL) which depends on the enantiomer. Chiral molecules and nanoparticles can rotate the polarization plane of the linearly polarized light and, conversely, phase offset the left and right components of CPL. This wavelength-dependent effect is known as optical rotatory dispersion (ORD) [20–23]. The optical activity phenomena ORD and CD are Kramers-Kronig–related [20]. VROA uses a difference in the intensities of the right- and left-handed circularly polarized scattered beams to identify chiral molecules by Raman spectroscopy.

The differential chiroptical effect of enantiomers is weak and often constitutes only one part in 10^4- 10^6 of the total optical response that the corresponding racemic mixture will have on the incident light beam. Furthermore, for many molecules, the most significant chiroptical signal is often located in the UV spectral range around 150–300 nm, where we often find the molecular absorption bands. The result is a poor chiroptical response for many of the commonly-used chiroptical spectroscopies such as CD, ORD, and VROA [24,25]. A large amount or a high concentration of chiral molecules is often needed for chiroptical spectroscopic analysis. Furthermore, it is often complicated to separate the chiroptical signals of a mixture of chiral molecules [20].

Fortunately, chiroptical molecular signals can be enhanced by plasmonic nanoparticles and nanostructures. For example, the LSPR-based sensors for detecting chiral molecules enhance the intrinsic CD signal of the molecule itself, or they provide an additional plasmon-enhanced chiroptical signal which appears in the CD spectrum at or near the plasmon resonance wavelength [20,26]. Enhancing chiroptical signals with plasmonic nanoparticles and nanostructures has already found a wide range of applications in the sensitive detection of chiral molecules. For example, the chiral plasmonic nanostructure can provide a large sensitivity enhancement for detecting molecules with optically active absorption bands that lie in the ultraviolet (UV), visible, and infrared (IR) spectral ranges [22,23,25,27–30]. Besides sensing, chiral plasmonic nanostructures have been used as excellent tools for the optical trapping and manipulation of micro/nanoparticles, as well as molecules [31]. For example, plasmonic nanostructures that were illuminated with circularly polarized light have been shown to rotate microparticles [32]. More recently, it has been proposed that optical forces could selectively manipulate and detect chiral molecules [33–35].

The chiroptical sensing and manipulation of molecules and nanostructures is a highly active field. The reason for this is that we do not yet have a complete theory that describes all the optical interactions that take place between a (complex) plasmonic nanostructure and the chiral molecule. It is challenging to predict the plasmon-enhanced chiroptical signals, their plasmon-enhanced sensitivities, and associated chiroptical forces [20,36]. Fortunately, the most recent advances in a more precise top-down and bottom-up assembly and fabrication of plasmonic micro and nanostructures allow a more careful exploration of the intricate optical physics of plasmonic nanostructures and their interactions with chiral molecules. In addition, highly sensitive interferometric methods are emerging, such as those based on combining plasmonic nanoparticles with optical microcavities, and they provide an unprecedented level of sensitivity for detecting single-molecule interactions with plasmonic nanostructures. This bodes well for a detailed study of their intricate chiral optical interactions [11,13].

Here, we provide the researcher entering the area of chiroptical sensing with a timely review of the established techniques and the most recent advances in sensing and manipulation of chiral molecules and nanostructures. We focus on chiroptical sensing techniques that can be enhanced by plasmonics, enabling sensitive detection and highly controlled manipulation capabilities. We highlight some of the seminal contributions to the field and point to the most exciting, and the most practical applications. In this context, we also review the fabrication and assembly of (dynamic) chiral plasmonic nanosystems which can be used for molecular sensing and manipulation. In closing, we discuss the challenges for sensing and manipulating chiral molecules and chiral nanostructures that the field may address using the emerging (dynamic) plasmonic nanostructures and the plasmon-based ultra-sensitive detection schemes.

This review is structured as follows: We first review chiral sensing techniques, reviewing the established spectroscopy techniques first and then focusing on the emerging plasmon-enhanced sensing approaches. Next, we review the optical manipulation of chiral molecules and nanostructures and summarize the recent developments that enable the study of handedness selective forces. We review the fabrication and assembly of chiral nanosystems and those that can be reconfigured. We close with a discussion on the future directions the exciting field of plasmon-enhanced chiroptical sensing and manipulation may take.

2. Sensing of chiral biomolecules

As we already discussed in the introduction, chirality is a characteristic of almost identical molecular structures called enantiomers which have non-superimposable mirror images [37]. The enantiomers of a chiral molecular structure often possess remarkably similar physical properties. Therefore, the methods which are commonly used for separating chemicals are often unsuitable for direct application in separating the pair of enantiomers. The challenge lies in choosing an appropriate chiral selector, a material or molecule that interacts in an enantioselective way in preparative and analytical chemistry techniques [38]. For example, chromatographic methods have been used for detecting and separating enantiomers with appropriate chiral selectors such as the cyanuric acid- modified Carboblack C adsorbent that was used for separating enantiomers of 2-chlorobutane and 2-bromobutane [39]. There are always uncertainties in the separation process not only due to the imperfect workings of the chiral selectors but also because of the difficulty in precisely analyzing the composition of the prepared sample. Better chiroptical sensors and spectroscopies are needed for assessing the success of preparative analytical techniques and for assessing the quality of chiral selectors. Plasmonic nanoparticles and nanostructures can potentially provide the required enhancements of the chiroptical signals for a more sensitive analysis of chiral molecules [23,40,41].

Chiral optical sensing in general depends upon two important processes which are the chiral recognition by a chiral selector and the chiroptical signal transduction. A crucial step when developing a chiral sensor is often the judicious choice of the molecular structure that is used for the specific recognition of the enantiomer. The chiral selector should provide highly enantioselective recognition sites to achieve a high chiroptical detection sensitivity and selectivity [42].

Chiroptical sensors can be distinguished by the diverse ways in which they transduce the chiroptical signal. We categorize the most prominent chiral sensors into three main sensor types: fluorescent chiral sensors, colorimetric chiral sensors, and CD signal-based sensors. Fluorescent chiral sensors transduce the chiroptical signal by fluorescence quenching or fluorescence enhancement, colorimetric sensors show changes in a UV–vis absorption spectrum, and CD signal sensors respond to chiral molecules with changes in their CD spectrum [40]. In the next section, we consider some of the chiroptical sensors for each of these categories of chiral sensor. We highlight some of those sensors which have demonstrated impressive chiral sensing capabilities, and those that have shown improved detection limits with the use of plasmonic nanoparticles and nanostructures.

2.1. Fluorescent chiral sensors

Fluorescent chiral sensors are often composed of chiral selector materials to recognize and differentiate the enantiomers. The chiroptical signal most often results from a quenching of fluorescence light emission. Semiconductor nanoparticles such as quantum dots (QDs) have been widely investigated as the fluorescent emitters as part of fluorescent chiral sensors [43–45]. QDs generally exhibit high quantum efficiencies, chemical stability and size-dependent wavelength tunability. For example, the specific detection of carnitine enantiomers was demonstrated with L-cysteine (L-Cys) and D-cysteine (D-Cys) capped CdSe(ZnS) QDs [44]. The fluorescent signal of L- Cys capped QDs decreased when D-carnitine was added to the sample, whereas no such change in the fluorescence signal was observed for the D-Cys capped QDs. Conversely, the fluorescence signal of D-Cys capped QDs was quenched by the addition of L-carnitine while no such effect was observed for the L-Cys capped QDs.

Cadmium sulfide (CdS) QDs have been used as the fluorescent probes in glucose biosensing based on CD spectroscopy [43]. Cysteamine-capped CdS QDs were mixed with D-penicillamine (DPA) to prepare chiral QDs. The DPA made the cysteamine capped CdS QDs optically active and detectable in CD spectroscopy. The enzyme glucosidase catalyzes the oxidation of glucose which results in the production of H_2O_2, a highly reactive chemical that destroys the chiroptical signals associated with DPA QDs. A decrease in the CD signal was observed as a function of increasing glucose concentration. The authors reported a selective detection of glucose with a detection limit of ~31 µM, over a concentration range up to 250 µM under the optimized conditions.

Chiral sensing from fluorescence intensity changes in complex assemblies of QDs was demonstrated for the enantioselective detection of cysteine [45]. L-Cys and D-Cys modified CdTe QDs and gold nano-rods that were used in a mixture to probe for trace amounts of cysteine that was added to the mixture. The addition of an exceedingly small amount of cysteine resulted in the formation of tight nanoparticle assemblies (i.e. of the L-Cys modified CdTe QD with the gold nanorods), selectively for only one of the two enantiomers. The energy transfer from the QDs to the gold nanorods resulted in enantiomer-specific quenching of the fluorescence signal. By comparing the fluorescence response of the L-Cys and D-Cys modified QDs, it was possible to quantify the composition of a cysteine sample down to an enantiomer excess ratio of 9:1.

2.2. Colorimetric sensors

Many colorimetric chiroptical techniques exploit LSPR for signal enhancements. Colorimetric detection by absorption spectroscopy is simple, can be extremely sensitive, enantiospecific, and low cost. Colorimetric chiral sensors have been used to detect oligonucleotides [46,47], small molecules and aptamers [48,49], proteins [50], carbohydrates [51] and metal ions such as lead [52,53], all mostly in homogenous solutions. Often it is possible to observe the colorimetric changes directly with the naked eye, adding to the importance of this approach to achieve rapid and low-cost sensing assays [54,55].

One example of a highly-sensitive, plasmon-enhanced colorimetric chiroptical sensor utilized uridine 5'-triphosphate (UTP) – capped silver nanoparticles (AgNPs) for the detection of L- and D-cysteine [56]. AgNP was chosen as the color reporting element because of its pronounced and narrow plasmonic absorption spectra and extinction coefficient, which is higher compared to many other plasmonic metal nanoparticles of comparable size and shape for example those based on AuNP. Capping agents were added to stabilize the AgNP. This work explored nucleotides UTP and ATP as the capping agents which are both known to make interactions with Ag via their nucleobase and/or phosphodiester chemical groups. The phosphate group, which is negatively charged, further helps in the stabilization of the nanoparticles against aggregation during the nanoparticle growth in solution.

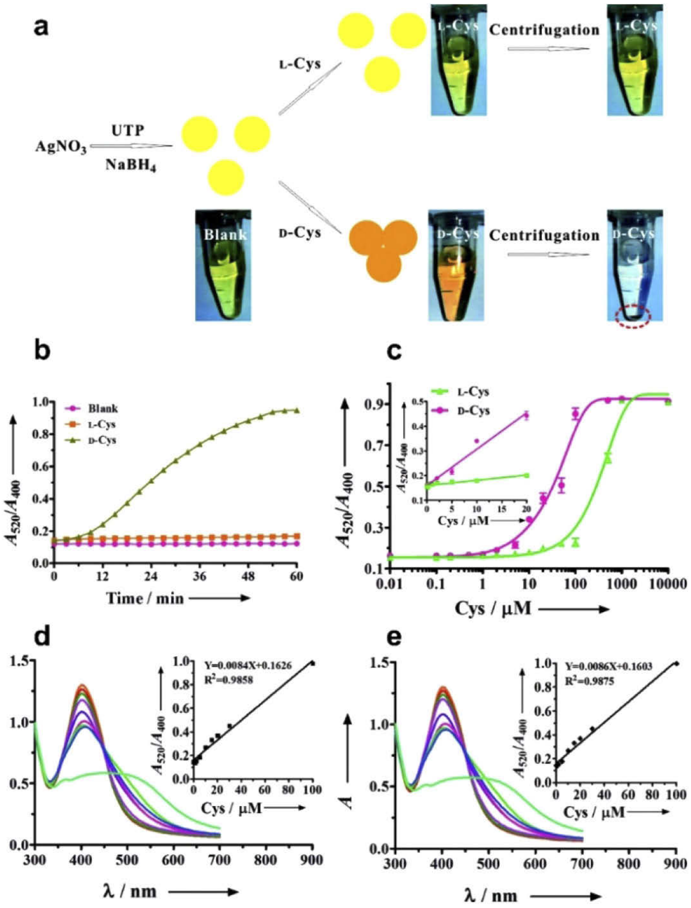

Fig. 1. (a) Colorimetric detection and discrimination of L- and D-cysteine using UTP capped AgNPs. (b) Plots of absorbance ratio (A_{520}/A_{400}) of UTP coated AgNP, corresponding to blank (H_2O), 100 μM L-Cys and 100 μM D-Cys for a period of 1 hour. (c) Plots of absorbance ratio of UTP coated AgNP with varying concentrations of L-Cys and D- Cys. Magnification of the plot in the range 0 to 20 μM is shown in the inset. UV-vis absorbance spectrum of ATP capped AgNPs in solution upon addition of (d) L-Cys and (e) D-Cys as the control experiments. Reprinted from Ref. [56].

Figure 1(a) shows the colorimetric detection and discrimination of L- and D-Cys by the UTP-capped AgNPs. The visible colorimetric shift from yellow to red was observed for the UTP capped AgNP in the presence of D-Cys, and no such pronounced color change was observed for L-Cys. The enantioselective detection was made possible by the selective interaction of the UTP capped AgNP (the chiral selector) with D-Cys. The absorbance ratio (A_{520}/A_{400}) had been selected as the performance indicator for the chiral sensing and was related to the ratio of dispersed to aggregated AgNPs. The time course of the absorption characteristic of UTP capped AgNP when interacting with D-Cys and L-Cys was observed to be conspicuously different, as shown in Fig. 1(b).

D-Cys seemed to selectively interact with the UTP capped AgNP and this led to their aggregation. Figure 1(c) shows the calibration curve for the absorbance ratio A_{520}/A_{400} measured for varying concentrations (up to 10 mM) of L-Cys and D-Cys. It was observed that the onset of AgNP aggregation induced by D-Cys occurred for concentrations much lower than for L-Cys, by two orders of magnitude. The limit of detection for discriminating L-Cys and D-Cys with this method was approximately 100 nM. As control, the authors used ATP for stabilizing the AgNP. With the increase in concentration of L-Cys and D-Cys, there is a gradual decrease in the absorbance at the short wavelength band around 400 nm, as shown in Fig. 1(d), and gradual increase in the absorbance around 520 nm, which is shown in Fig. 1(e). Although the absorbance ratio was responsive to the cysteine concentration, the ATP capped AgNP was found not to be a good selector suitable for discriminating the L-Cys and D-Cys enantiomers.

2.3. CD based chiral sensing

Chiral supramolecular architectures are ubiquitous in nature and a prominent example of this is the helix-shaped tobacco mosaic virus (TMV) which is found in plants, shown in Figs. 2(a) and (b). The chiroptical characteristics of the CD spectra of a complex aggregate made of TMV decorated with AuNP has been investigated in [57]. AuNPs of size of ~5 nm were bound to the TMV using a peptide, the titanium-binding peptide (tbp) that is located at the surface of the TMV helix. TMV was genetically modified to express tbp. CD spectra of TMV-Au NP for wild type TMV (blue) and tbp-TMV (red) are shown in Fig. 2(c). Strong CD signals were measured for the tbp-TMV-Au NP complex in the UV spectral region. The CD peaks arise from the chiral structures of molecular complex of TMV and the inherently achiral AuNPs. Optical activity was enhanced at two different wavelengths (540 nm and 222 nm) when AuNPs were attached to TMV.

In numerical finite-difference time-domain simulations, strong CD signals are obtained from chiral medium patches (molecules) that are placed within the gap of a dimer nanoantenna. The chiroptical signal is enhanced by induced CD [59]. The strongly localized plasmonic near-field that is overlapping with the chiral medium patches plays the key role in the CD signal enhancement at the wavelength of the plasmon resonance. The CD enhancement factor, defined as the ratio between the absolute values of the CD signal of the chiral medium patches alone, and with plasmonic antennas, can be as high as 10^3 [60] . This pronounced CD signal enhancement factor is observed in numerical simulations when the two-rod nano antennas are aligned along their long axis such that they interact with the chiral medium patch located within the gap formed between them [60]. In this case, the intensity enhancement in the gap is about 4 times higher as compared to the enhancement of the single rod nanoantenna, for a gap size of 5 nm. It is interesting to note that a standard planar parallel-aligned gap antenna dimer delivered a CD enhancement factor that was higher than that of a single rod nanoantenna and that of the Bohn-Kuhn-type nanoantenna dimer geometry. In the Born-Kuhn-type nanoantenna geometry, the two antennas are arranged in orthogonal and chiral fashion as corner-stacked gold nanorods [61]. Nestrov et al. have reported that the CD enhancement factors are highest for those nanorod antenna dimer configurations in which incident and hotspot electric field vectors are parallel to one another, and when simultaneously the average field enhancement value is high [60]. Similarly, elevated levels

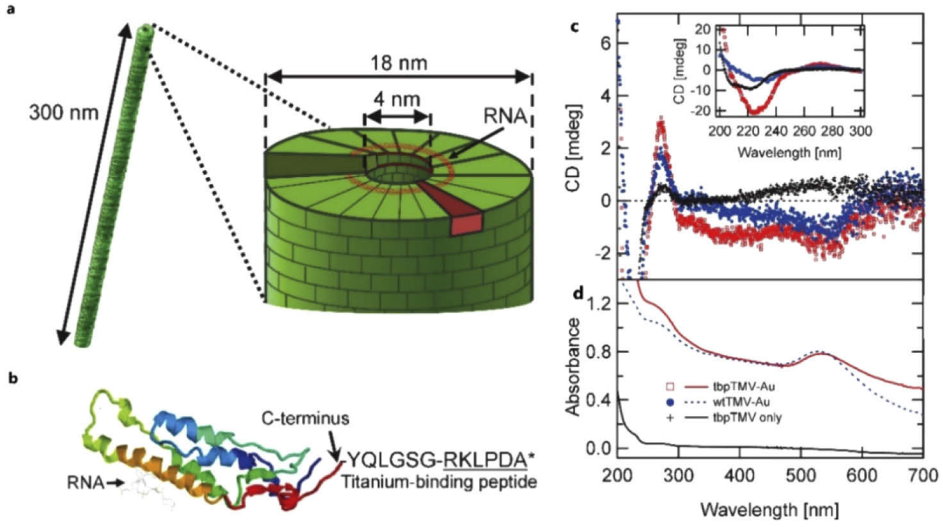

Fig. 2. (a) The TMV virus has a right-handed helical form with 16 and 1/3 coat proteins representing each helical turn. The proteins are oriented along the RNA of this plant virus. (b) Pymol (a molecular graphics system) illustrated coat protein subunit of the virus (PDB:2OM3) [58]. C terminus of the coat protein, a wild type (wt) protein is fused with titanium binding peptide (tbp), an amino acid sequence. (c) CD spectra obtained from tbp TMV-Au (red open squares) and wtTMV-Au (blue filled circles). Black crosses indicate tbp TMV only. Enlarged spectra between 200 and 300 nm are shown in the inset. (d) UV-vis spectra of the complexes measured at the same time. Reprinted from Ref. [57].

of induced CD signal enhancements have been observed for nanoparticle assemblies with cholate coated silver nanoparticles [62], nanospheres [63,64] and cysteine coated gold nanorods [65,66], for example. Strong CD signals were obtained from the end-to-end assembly of plasmonic gold nanorods by cysteine and glutathione and excited in the visible region (500–850 nm) [66]. The chiral currents that are generated inside the gold nanorods account for the strong CD signals. This distinctive chiroptical sensor achieved a detection limit down to micromolar concentrations and showed good selectivity towards cysteine and glutathione in the presence of other amino acids.

Plasmonic dimers enabled the detection of small chiral molecules with a good sensitivity. The detection of bisphenol A (BPA, MW∼228 g/mol), an endocrine disrupting chemical detrimental to human health, has been detected with a detection limit of 0.02 ng/ml based on the formation of asymmetric plasmonic dimers [67]. The sensing mixture contained the pre-assembled plasmonic dimer particles composed of one AuNP particle coated with an anti-BPA antibody (Ab) and one AuNP coated with BPA. These particles form AuNP dimers which were disrupted when free BPA was added to the solution. The decrease of the CD signal at 533 nm corresponded to the amount of BPA in solution. BPA solutions of different concentrations were added to the AuNP dimers and subjected to CD spectroscopy.

Various other analytes have been detected by tailoring the chiroptical response obtained from the assembly/disassembly of plasmonic nanoparticles in the presence of chiral molecules [23]. For example, silver ions were detected with a detection limit of 2 pM by activating a nanoparticle dimer assembly reaction [68]. Plasmonic nanoparticles are modified with short pieces of DNA that contain cytosine. Adding Ag^+ ions led to the association of two plasmonic particles species, each modified with cytosine-containing non-complementary DNA oligonucleotides. The metal-mediated base pair formation (cytosine-Ag^+-cytosine) resulted in the DNA hybridization and the formation of plasmonic nanoparticle heterodimers resulting in the strong induced CD signal in the presence of Ag^+ ions.

Ochratoxin A (OTA), one of the most poisonous mycotoxins, has been detected with an excellent detection limit of 0.16 pg/ml by a heterogeneous system that uses an Au core and Ag satellite nanoparticles assembled into a detection complex [69]. The Au core Ag satellite complex was assembled by modification of the nanoparticles with complementary DNA oligonucleotides. One of the oligonucleotides was an OTA aptamer. Adding OTA resulted in disassembly of the complex and reduction of the CD signal. In another example, DNA was detected at zeptamolar concentrations by using multimetal shell-engineered nanoparticle assemblies [70].

A simple and sensitive CD spectroscopic method was developed for the detection of 8-OHDG (8-hydroxy-2'-deoxyguanosine) in human serum using assemblies of DNA-modified AuNPs [71]. 8-OHDG is a well-known biomarker for oxidative DNA damage. AuNPs of sizes 25 nm and 20 nm were modified by oligonucleotides and assembled into dimers with strong CD enhancement. One of the oligonucleotides was an 8-OHDG aptamer. Adding 8-OHDG to the nanoparticle assembly resulted in a decrease of a strong CD signal in the visible around 550 nm, as shown in Figs. 3(a) and (b). In the UV-vis absorbance spectrum, the change of 8-OHDG concentration had no noticeable effect, signifying the more sensitive detection performance of induced CD spectroscopy compared to the UV method, as shown in Fig. 3(c). The CD modus operandi was used for the detection of 8-OHDG with a detection limit of 33 pM and over a linear range of 0.05 nM to 2 nM.

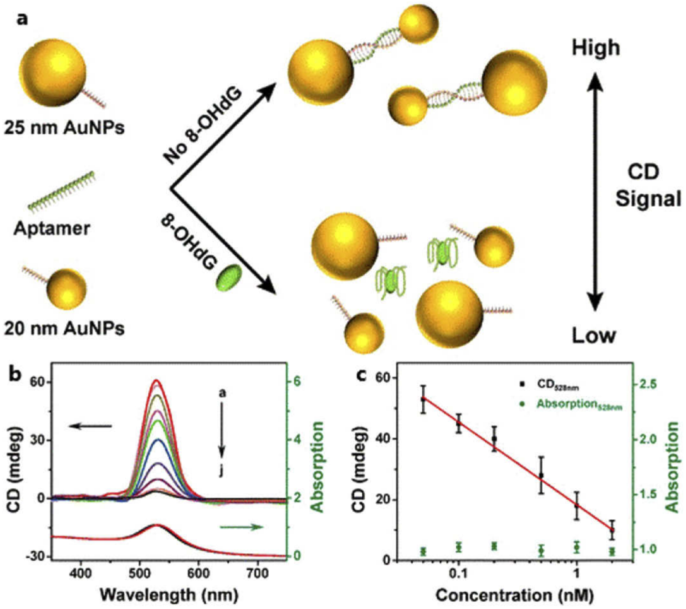

Fig. 3. (a) Mechanism for ultrasensitive detection of 8 OHDG via chiroplasmonic assemblies of AuNPs. (b) CD and corresponding UV−vis absorption curves with different concentrations of 8-OHDG. (c) CD intensity was in log−linear correlation with the concentration of 8-OHDG ranging from 0.05 to 2 nM. Reprinted from Ref. [71].

2.4. *Other chiroptical transducers, spectroscopic and imaging methods*

A circular dichroism imaging microscope (CDIM) has been constructed in [72] to uncover the heterochiral domains in biaxial dye crystals. This heterogeneity is concealed by conventional X-ray scattering and obscured by linear birefringence (LB) and linear dichroism (LD). In earlier studies of anisotropic samples by CD microscopes [73], researchers came across instrumental artefacts [74] arising from electronic polarization modulators that create sinusoidally varying polarization states. This resulted in the mixing of linearly polarized light into the circularly polarized output. However in [72], the authors reported a retrogressive approach to eschew the usual linear biases with electronic circular polarization modulation, creating CD images at the same time. The visible light CDIM as shown in Fig. 4(a) has been built based on mechanical light modulation by rotating a linear polarizer with respect to a quarter wave plate. The quarter wave plate is tuned continuously by tilting to the required wavelength. This technique came up with near perfect circular input by signal averaging with a charge coupled device (CCD) camera. A depolarizer, sliding interference filter, and Glan Thompson polarizer are fixed to the motor and the tilting λ/4 plate is staged below the sample stage of a microscope. In order to obtain the CD measurements on oriented samples, the polarizer is alternatively directed between +45° and −45° polarization states with respect to the extinction directions of a λ/4 retarder that is modulated by tilting. Tilting the retarder results in changing elliptic cross section passed over by the incident light, finally altering the effective birefringence of the retarder. This guaranteed the stability of right and left circularly polarized light (which are alternating) generated at all wavelengths chosen by the variable interference filter.

To check the feasibility of the CD microscopy, the authors used a sample of crystalline 1, 8-dihydroxyanthraquinone (DHA) as shown in the inset of Fig. 4(a). The crystal was put up on large (0.5 cm × 0.5 cm × 100 µm) square plates formed by the evaporation of acetone/acetonitrile solutions. The crystal was kept in the center and along the borders between lateral growth sectors. Figure 4(b) and Fig. 4(c) show the mirror image domains as a red heterochiral spin wheel where CD is positive and a blue heterochiral spin wheel where CD is negative. Blue pin wheels were oriented in the counterclockwise direction and red pin wheels were oriented in the clockwise direction, signifying the crystals tend to grow in one direction. The images obtained were independent of sample rotation and the best way to eliminate the linear biases in the optical train.

CD is observed to be sensitive to the helical confirmation of molecular assemblies and (bio) polymers. A two-photon fluorescence (TPF) scanning confocal microscopy was combined with 2D imaging of CD, to map the spatial distribution of the nonlinear CD properties of polymer samples [75]. This combined technique might provide significant information about microscopic molecular organization. Thin films of a chiral, π-conjugated polyfluorene, poly [9,9-bis((3S)−3,7-dimethyoctyle)−2,7-fluorene] was chosen as a candidate to demonstrate the potential of CD-TPF microscopy. Two different imaging modes, a static mode and a dynamic mode were executed in order to probe the spatial distribution of the CD in the sample. A quarter wave plate was used to excite the sample with left hand circularly polarized (LCP) light and right hand circularly polarized (RCP) light in the static imaging mode. The images of the two circularly polarized states of light are recorded with a photomultiplier as the detector. A photoelastic modulator (PEM) regulates the excitation beam between LCP and RCP in the dynamic mode. TPF was produced using a photomultiplier in current mode and lock-in signal demodulation. Even though the static mode was obtained with finer sensitivity, it was more sensitive to long term drifts due to the laser power that could occur during the acquisition of the image. At the same time, the dynamic mode needed a modulation-demodulation scheme but was less affected by mechanical and power drifts. This mode did not require any further processing on the images acquired. Figures 4(d) and (e) represents the 2D maps of g_{TPF} (dissymmetry factor of the TPF signals) using dynamic and static modes respectively. The map of the transmission CD dissymmetry factor is shown in Fig. 4(f). The g_{TPF} exhibits spatial variations and $|g_{TPF}|$ varies between 0 and 0.07, which is more than 1 order of magnitude larger than the detection limit. The authors reported the sensitivity of the apparatus is good enough for the quantitative evaluation of small chiroptical effects. The blue and red zones indicate the difference in sign of the g_{TPF}

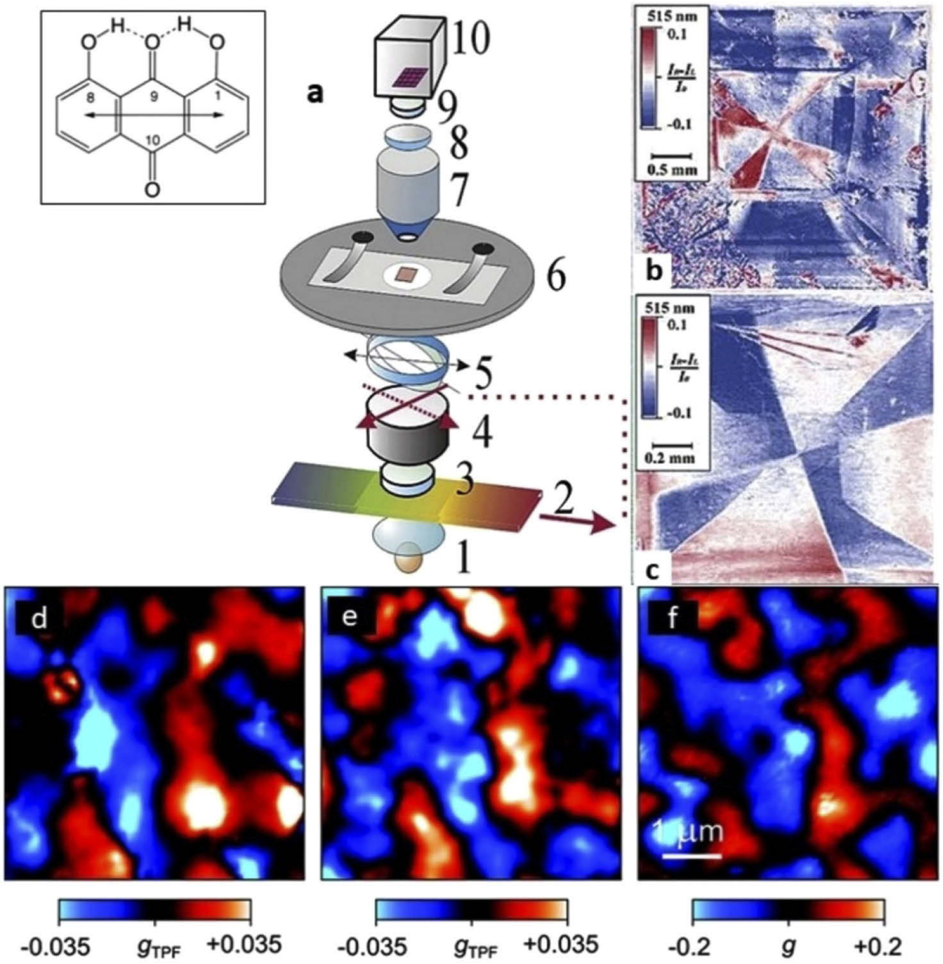

Fig. 4. (a) Visible light CDIM (1) Light source, (2) Variable interference filter, (3) depolarizer, (4) rotating polarizer, (5) tilting $\lambda/4$ compensator, (6) sample mount, (7) objective, (8) projector lens, (9) depolarizer, (10) CCD Camera. The inset shows the structure of DHA with the electric dipole moment indicated. (b) CD image of a crystal recorded at 515 nm. (c) Heterochiral pinwheel shown in the CD of the center of another crystal. Reprinted from Ref. [72]. The dissymmetry factor g_{TPF} for the TPF signal excited at $\lambda = 830$ nm and gathered in (d) dynamic mode (e) static mode. (f) the dissymmetry factor g for the CD transmission at $\lambda = 405$ nm in dynamic mode. Reprinted from Ref. [75].

in the nearby areas. The researchers emphasized the importance of CD-TPF microscopy to differentiate between the two different structural chiral configurations, and that it has remarkable significance in various situations where a multiphoton spectroscopy method bestows favorable imaging properties.

Raman Optical Activity (ROA) can be extremely sensitive to the chirality of a molecule or a molecular complex and can be used to determine a molecular configuration or conformation. ROA has been used as a unique and distinct tool for analyzing spectral patterns for the detection of peptides, proteins, glycoproteins, and intrinsically disordered proteins [76–79]. Normally, Raman spectra of proteins emerge from the backbone and the flexible side chains of the protein. In contrast, the ROA spectra contain information about the amide bonds and the skeletal stretching vibrations of the backbone of the protein, thereby providing a better understanding of the secondary structure of a protein [80]. ROA analyses the differences in Raman spectra, comparing the Raman signals that are obtained separately for the excitation by right- and left- hand CPL. The drawback of ROA lies in the difficulty of obtaining a detailed interpretation of the scattering spectra. Furthermore, ROA possess certain limitations due to the low scattering intensities. ROA intensity is often only 10^{-3}–10^{-5} times that of the Raman scattering intensity. LSPR enhancements can potentially resolve this inherent drawback of the ROA method. LSPR enhanced ROA was studied by Sun et al. with chiral molecule fmoc-glycyl-lysine-OH (FGGO) [81]. The circular intensity difference (CID), the dimensionless ROA parameter introduced by Barron and Buckingham [82], was enhanced with Ag nanowires. They showed, when the laser light was illuminated on the Ag nanowires and coupled with the nanoantenna, that the local and remote Raman intensity of FGGO at 1593 cm^{-1} was significantly enhanced by excitation with the left and right CPL.

With the recent broader availability of X-ray light generated in synchrotrons and the wider availability of X-ray free electron lasers, the infrared and nonlinear spectroscopic techniques can now be extended to the X-ray regime. The unique characteristic of the X-ray light-matter interaction is given by the spatially localized and element-specific resonance with core excitation in molecules. X-ray Raman optical activity (XROA) measures the optical activity of the valence electronic excited manifold accessible through intermediate core electronic excitations. Therefore, the chirality of molecular structure (where signals are particularly targeted) can be probed by this method. XROA on and off resonant signals have been predicted by Rouxel et al. [83]. XROA is essentially a version of Resonant Inelastic Scattering (RIXS) which is chiral sensitive. The authors simulated the XROA signals for L-tyrosine excited at N and O K-edges. The authors suggest that XROA is electric quadrupole-dependent for molecules which are oriented in any direction, and thus could be a boon for investigating molecular chirality.

Optical Rotatory Dispersion (ORD) was first observed by Biot in 1815 [84]. It is one of the commonly used chiroptical spectroscopic methods for characterizing chiral molecules. ORD is a property shown by chiral molecules or structures due to the variations in the propagation velocities when they are acted upon by left and right hand circularly polarized light. The plane of polarization of linearly polarized light is rotated in ORD. As is well known, a polarized plane wave can be decomposed into its left and right circularly polarized electric field components (E_L and E_R) respectively. A linearly polarized wave has its left and right components equal in magnitude. When a linearly polarized light passes through a sample which is chiral in nature, it shows both ORD and CD. But if the sample exhibits only ORD without CD, the left and right electric field components (amplitudes) rotate differently, keeping the magnitude of the amplitude constant. Quantitatively, ORD can be expressed in terms of refractive indices of the left- and right- hand CPL components propagating through the chiral molecule [85]. ORD can also be defined as the variations in the optical rotatory power of an optically active material with the variations in the wavelength of the incident light [86]. The polarizability of the optically active molecule changes with the wavelength of the incident light, therefore ORD can be plotted with incident wavelength on x axis and rotatory power on y axis. The characteristic of the plot gives a clear idea of the rotation, i.e., if the curve is in the positive the light rotates in a clockwise direction and light rotates in a counterclockwise direction when the curve is in the negative [22].

A state-of-the-art example for determining the ORD in aqueous solution of methyloxirane is given in Ref. [87]. Experimental evidence for optical rotation, dipole radiation and optical rotatory dispersion, which are challenging to visualize, have been shown in Ref. [88]. The authors observed dark and light bands that showed a variation in the polarization state of a linearly polarized light, when it is passed through a sucrose (chiral molecule) solution. Point particles that scatter light in the form of dipoles, provide visibility to the changes in polarization. The ORD of the medium generates a rainbow pattern of colors when a white light beam is passed through the sample. A broadband polarimeter setup to distinguish between glucose and albumin was developed based on the ORD properties of these optically active molecules [89]. The researchers examined the partial least squares (PLS) regression on the broadband rotation data in the wavelength range of 380–680 nm and were able to successfully differentiate the optically active substances based on their ORD. Glucose was combined with different concentrations of albumin to probe the spectral superposition. Varying albumin concentrations resulted in a standard prediction error of ±16 mg/dl. The authors suggest that the method could be used for better glucose prediction in the presence of albumin.

3. Handedness-selective optical forces

In chemistry, the sorting of substances by their chirality must be addressed through the introduction of a specific chiral resolving agent, as is, for example, the case in chiral chromatography using a chiral selector. The chemical sorting processes, may however introduce unwanted side products and, more importantly, most often have a low enantiomer selectivity and a poor atom economy [90]. Finding chiral separation methods without depending on a chiral material environment remains a challenge. More recently, electromagnetic techniques have been shown to be a powerful alternative to the chromatographic separation methods. In these novel optical approaches to chiral sorting, light can be less invasive than chemical methods and, in some cases, more effective in separating the enantiomers [91–93].

3.1. Theory and simulation of optical handedness-dependent forces

Circularly polarized light carries angular momentum due to its intrinsic spin angular momentum. By coupling this momentum into chiral particles, forces can arise that separate the particles into different directions according to their handedness [94,95]. In the year 2014, Wang and Chan predicted that electromagnetic plane waves can exert lateral optical forces on chiral particles located above a reflective surface [64]. They simulated a linearly polarized plane wave illuminating a chiral structure located about 10 nm above the substrate which can be metallic or dielectric, see Fig. 5(a). Using the Maxwell stress tensor method, the lateral force experienced by the helical gold particle (inner radius 50 nm, outer radius 150 nm and pitch 300 nm) can be calculated. It acts in a direction where there is neither a wave propagation nor an intensity gradient and deflects particles with opposite helicity in the opposite direction. The lateral force can reach 0.4 times that of the forward scattering force if the gold helix is placed directly above a gold substrate. This counter-intuitive force results from the interaction between the particle and the reflection of its scattered field. In addition to its importance in basic research, this force may be useful for all-optical enantiomer sorting. Around the same time, Bliokh et al. published another way to generate a similar lateral force [96]. They simulated an achiral Mie-sized gold nanoparticle placed within an evanescent field of a prism in water. The evanescent field results from a polarized propagating beam that is total internal reflected at the prism surface. They found that a lateral force was generated because of transverse momentum and spin, as shown in Fig. 5(b). They revealed that the evanescent electromagnetic wave offers a rich and highly non-trivial structure for the local momentum and spin distributions. They found that the evanescent wave carries helicity-independent transverse spin and helicity-dependent transverse momentum, which provides the possibility for the chiral sorting of Mie particles and molecules. Chiral particles/molecules placed in the evanescent field should experience a force pointing in the opposite direction according to their chirality [96]. In 2015, Hayat et al. investigated a similar model for chiral separation. Instead of using an achiral nanoparticle they numerically simulated the lateral force on chiral materials in the evanescent fields [97]. They found that the strength and direction of the lateral forces are dependent on the chiral polarizability for example of a helicene molecule, which is shown in Fig. 5(c). They calculated the lateral optical forces in two sets of illuminations: one for the particle placed in the evanescent field, and the other for the particle placed in the plane wave above a surface. The results showed that chiral particles experience a higher force in the evanescent field. In their theoretical approach the lateral optical forces are much stronger than previously predicted ones due to the chiroptical response of the chiral particle. A force with a magnitude around $10^{-19} N/(mW/(\mu m^2))$ was calculated for the helicene chiral molecules.

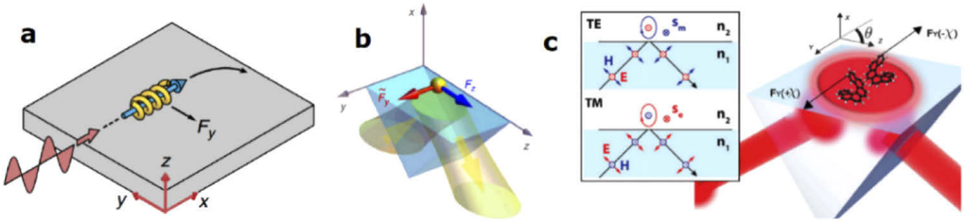

Fig. 5. (a) A linearly polarized plane wave irradiates a helix particle on a substrate and produces a lateral force. The arrows associated with the helical particles indicate the handedness. Reprinted from Ref. [64]. (b) A polarized propagating wave undergoes total internal reflection at the glass–water interface of a prism, thereby generating the evanescent wave extending into surrounding water. A gold spherical particle is placed in the water on the glass surface, and its observable linear and spinning motion is proportional to the forces and torques exerted by the evanescent wave. Reprinted from Ref. [96]. (c) Chirality-dependent lateral forces in an evanescent field. Particles in an evanescent field with transverse spin angular momentum experience lateral forces depending on their chiral polarizability χ, with particles with opposite helicities experiencing lateral forces in opposing directions. (Inset) Total internally reflected TE and TM waves give rise to evanescent waves that have transverse spin due to their elliptically polarized magnetic (TE) and electric (TM) fields. Reprinted from Ref. [97].

3.2. Theory and simulation of plasmonic enhanced optical chiral sorting forces

Due to the generally weak nature of the optical force exerted on nano-sized objects, chiroptical experiments thus far have only been able to separate particles that are micron-sized. For the nano-scale sorting of molecules, the expected optical forces are exceedingly small, their magnitude scales with the inverse of the polarizability of the particle. As a rule of thumb, the chiroptical forces are proportional to the volume occupied by the particle/molecule. Because of this, the chiroptical forces acting on nanometer-sized molecules are 9 orders of magnitude smaller as compared to the forces acting on micron-sized particles. The chiroptical forces acting on molecules are most likely always too weak to completely overcome the Brownian motion and other thermal effects in a solution, which makes their observation in an experiment extremely challenging. Observing the weak chiroptical molecular force is one of the great challenges when trying to take a first step towards sorting of chiral molecules with light.

In 2015, Alizadeh and Reinhard combined the ideas of optical chiral sorting and plasmonic enhancement [98]. Similar to the design from Bliokh and Hayat et al. [96,97], but instead of using optical excitation, they employed the surface plasmon polaritons (SPP). The plasmonic enhancement boosted both the gradients of the electromagnetic field as well as of the optical chirality, Fig. 6(a). Not only did they find that the lateral spin angular momentum of the chiral surface plasmon polaritons (excited by a metal nanoparticle sitting on a metal surface and itself excited with a circularly polarized light) caused the chiral objects with different handedness to experience lateral optical force in the opposite direction, but they also managed to calculate the force map along the two directions. At certain optimal position, the lateral forces exerted on chiral plasmonic nanoparticles are about $5pN/W$ and $-10pN/W$ for right and left-handed chiral nanospheres, respectively. Compared with the force calculated on a helicene chiral molecule by purely optical methods from Hayat et al., which is around $10^{-19}N/(mW/\mu m^2) = 10^{-4}pN/(W/\mu m^2)$ [97], one can observe an elevated force originating from plasmonic enhancements, which gives great encouragement for the feasibility of the plasmonic approach to chiroptical sorting of single molecules. However, to place a molecule at the maximum of the chiral force would require high precision in molecular positioning and this might be hard to achieve. A stable and precise (optical or electrostatic) trap for the molecules might be required to demonstrate such an experiment.

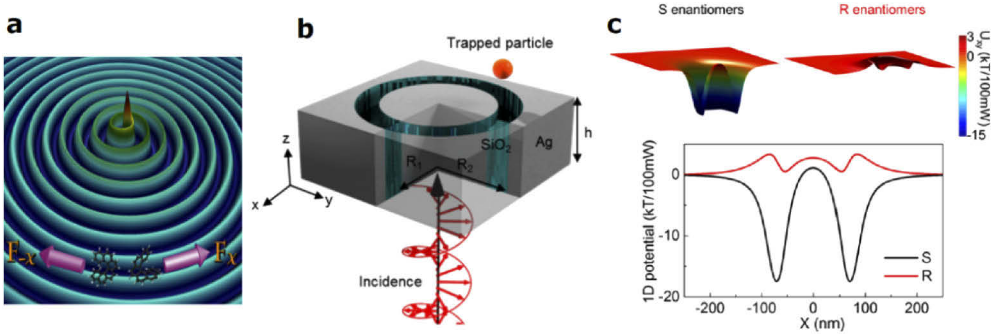

Fig. 6. (a) Schematic display of different forces exerted on a chiral helicene molecule by chiral surface plasmon polaritons. Reprinted from Ref. [98](b). Schematic view of the plasmonic coaxial aperture. The incident light is left-handed circularly polarized and propagates along the z direction. (c) Corresponding 2D and 1D trapping potentials with left-handed circularly polarized illumination. Distinctions of potentials between the S (black curves) and R (red curves) enantiomers provide selectivity to trap only one enantiomer. Reprinted from Ref. [35].

Saleh and Dionne proposed a plasmonic nanostructure that can be used as a low-power optical trap and which, in theory, could trap sub 10 nm dielectric particles while keeping the trapping power level below 20 mW [99]. The shape of the plasmonic coaxial aperture is shown in Fig. 6(b). This type of structure provides a steep trapping potential that is larger than 10 kT, which would be enough to oppose the Brownian motion of the trapped dielectric nanoparticles as small as 2 nm. A few years later Zhao et al. employed this coaxial nano-aperture structure in their theoretical work [35] that explored the selective trapping of chiral nanoparticles. In their numerical simulations they showed that the plasmonic coaxial aperture should be able to trap and manipulate sub-20 nm achiral particles. More importantly, when using circularly polarized illumination and chiral particles (20 nm diameter), the coaxial aperture should be able to stably trap S enantiomers with matched handedness of the incident light within 20 nm from the aperture, while the R enantiomers will not be trapped due to the positive trapping potential calculated at the same location, see Fig. 6(c). They model their targeted chiral specimen as a spherical nanoparticle with a diameter of 20 nm, a dielectric constant of 1.45 and a chirality κ −0.6 (R) and +0.6 (S) corresponding to an electromagnetic polarizability of $\sim 1.37/c \times 10^{-24)}m^3$, with c being the speed of light in vacuum.

3.3. Experimental research into plain optical chiral sorting forces

In 2011, Cipparrone et al. demonstrated tight-focus, light polarization handedness dependent forces [100]. In their experiment, they photo-polymerized cholesteric liquid crystals (CLCs) water emulsions into solid chiral microspheres, with the helicoidal structure and optical properties of the CLCs droplets preserved. They used optical tweezers as an illumination source and found that the same CLCs microparticle was applied to either trapping or repulsive forces depending on the handedness of input CPL. Later in 2013, the same group published the further study on the dynamics of the light-responsive chiral microparticles [101]. They found the origin of the optical forces can be explained by considering the interplay between the internal helical structure of the CLC and the CPL, where forces occur when the wavelength of the optical tweezer is of the order of the cholesteric spatial periodicity, due to a circular Bragg condition for which the light is selectively reflected. Further considering the reflection and transmission properties of the CLCs, optical gradient and scattering forces can be evaluated, see Figs. 7(a) and (b). In 2014, they extended their work into polarization-dependent optical forces and torques mediated by the CLC microresonators [102]. Optical trapping forces and torques on L-chiral CLCs microparticles were measured and compared on an optical tweezer setup operating at wavelengths of 785 nm and 830 nm, with both wavelengths fulfilling the selective reflection condition. The optical forces and torques on the trapped particles were measured by detecting the thermal fluctuations and the light-induced rotations in the effective harmonic potential by back focal plane interferometry. The broken symmetry was shown to allow for selective reflection of CPL, thereby inducing the spin-dependent optomechanical force and torque effects.

Instead of applying a focused input beam, Tkachenko and Brasselet reported plane-wave-like light polarization handedness dependent forces [105]. They have employed transparent right-handed CLCs droplets as the chiral subject, where a strong coupling between linear and angular degrees of freedom of light can be expected. Two sets of experiments were carried out, one using a single beam to illuminate the droplet with on-axis CPL of left and right handedness states. The other experiment employed two coaxial counter propagating beams with equal power and waists to achieve full control of the optical radiation pressure exerted on the CLC droplets by a mere change of the photon spin. They found that the force exerted on the chiral droplet depended on the handedness of illuminating CPL. One year later the same group showed one of the first experiments that demonstrate the optical sorting of chiral materials [104]. They utilized chiral (cholesteric) and non-chiral (nematic) liquid crystal droplets with diameter around 15 µm. They first applied counter propagating CPL with left and right handedness onto an achiral (nematic) droplet (Fig. 7(g) top panel). Thus, the droplet particle felt the exact same forces from both sides and the optical forces cancelled each other. No matter the configuration of the illumination, the droplets did not change the straight trajectory they moved on, as shown in Fig. 7(g) bottom panel. However, when using a droplet composed of chiral (cholesteric) liquid crystal, the droplets changed trajectory depending on the handedness of both the illumination and the chirality of the liquid crystal, (Figs. 7 (f) and (h)). The authors chose Bragg CLCs droplets so that propagation of light in one of the two circular polarization states along the cholesteric helical axis was prohibited over a well-defined wavelength range; in this way the opto-mechanical separation of the droplets having opposing chirality could be enhanced and was observed at a low optical power. Importantly, the chiral sorting was also demonstrated in the case of non-Bragg CLCs chiral droplets. The origin of the force which changed the trajectory of the chiral droplets stems from either circular birefringence or circular dichroism. In Figs. 7(f)-(h) red arrows refer to the ‘Bragg optical rays’ that are totally reflected due to circular Bragg reflection over a certain circular

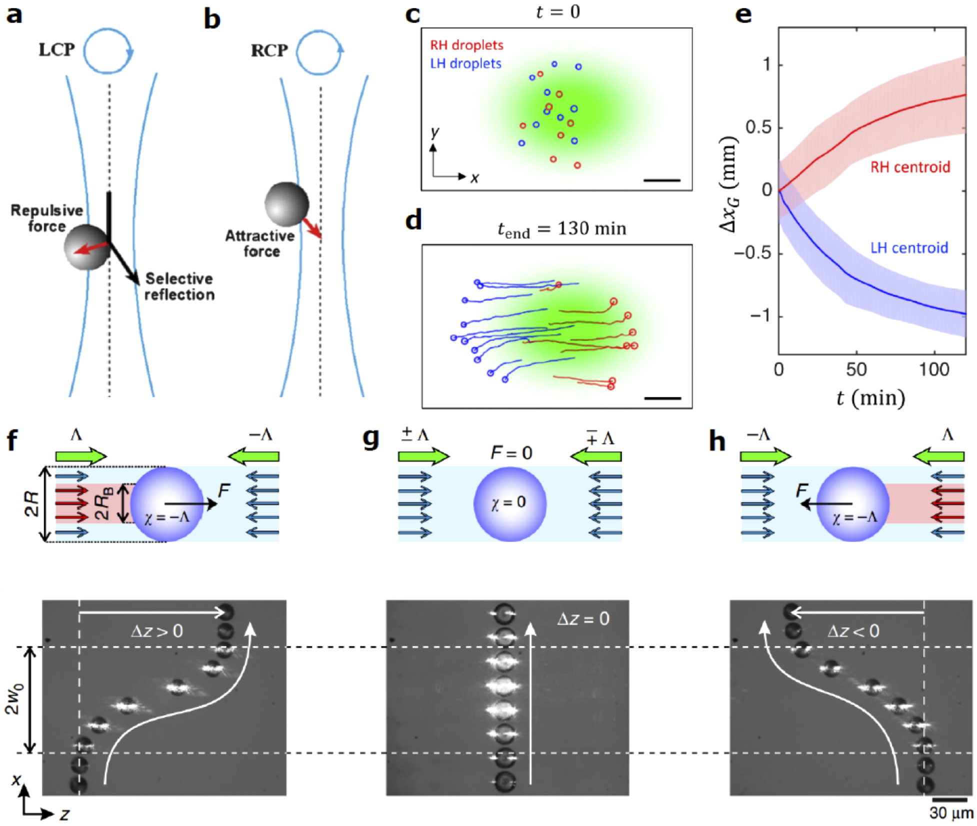

Fig. 7. Optical tweezers experiment onto cholesteric liquid crystals with (a) LCP and (b) RCP illumination. Reprinted from Ref. [101]. (c) The initial spatial distribution of the droplets (circular markers). (d) The location of the droplets after 130 min irradiation and individual trajectories. The Gaussian fit of the intensity cross section in the observation plane shown in green. Scale bars: 500 µm. (e) The dynamics of separation along the x axis of the left-handed (LH) and right-handed (RH) droplet centroids. Reprinted from Ref. [103]. (f, g, h) Top panel shows different light–matter interaction geometries, where two kinds of contributions to the net optical force F are identified for Bragg chiral droplets. Bottom panel: Demonstration of passive chiral optical sorting concept with chiral (f, h) and non-chiral (g) droplets that pass perpendicularly through the beams at a constant velocity along the x axis. The pictures are obtained by superimposing snapshots taken at a discrete set of time. Only chiral droplets experience a non-zero deviation Δz along the z axis that is proportional to $\Lambda\chi$, where χ=0 refers to non-chiral medium and χ=±1 to right/left-handed chiral media. Reprinted from Ref. [104].

cross-section of the droplet, whereas blue arrows refer to the ‘Fresnel optical rays’ that are refracted/reflected by the droplet as is the case for an isotropic non-chiral dielectric sphere. The results show that micron-sized chiral droplets/particles irradiated with circularly polarized light can feel different forces, which will drag them in opposite directions based on the handedness of their chiral constituents. It is worth emphasizing that in their experiment the microparticles were not chiral-shaped, and the sorting forces solely depend on the chirality of their liquid crystal constituents. At around the same time, work related to that of Cipparrone et al. [101] was shown by Tkachenko and Brasselet [106]. Instead of single CPL beam, they utilized dual focused CPL beam to for the selective trapping of CLCs microparticles with circularly polarized Gaussian or Laguerre–Gaussian beams. They demonstrated both experimentally and theoretically that the selectively trapping and repulsive forces are induced by the handedness of the CLCs.

More recently in 2019, lateral chiral forces have been reported by Kravets et al. [107] following their theoretical studies [95,108]. The experiments prepared a 1D gradient of helicity density light field by interfering two slightly noncollinear laser beams having orthogonal linear polarization states. CLCs microspheres are selectively displaced by means of optical forces arising from the optical helicity gradients. Kravets et al. have extended earlier work by Tkachenko and Brasselet [104] for a racemic mixture of chiral entities [103]. They experimentally demonstrated the handedness-selective mechanical separation of randomly distributed assemblies of CLCs microparticles by purely optical means. Commercial CLCs with different handedness were mixed and injected to a microfluidic device, and by the effect of carrier fluid, droplets are generated afterwards, an example is shown in Fig. 7(c). By utilizing two contra circularly polarized beams, chirality-selective displacement is then induced. The dynamics of the individual trajectories of the droplets are retrieved by analysis of the recorded video recordings, extracted trajectories are shown in Fig. 7(d). Figure 7(e) denotes the dynamics along the x axis of the left-handed (LH) and right-handed (RH) droplet centroids.

3.4. Experiments of plasmonic enhanced optical chiral sorting forces

The optical manipulation of molecules with the so-called optical tweezer technique has been demonstrated by concentrating the light on length scales beyond the diffraction limit using a variation of this technique with plasmonic nanoparticles in what is called the ‘plasmonic tweezer’ approach. Plasmonic nanostructures can localize the light on the length scale of macromolecules such as proteins (~3–10 nm) and thereby create enhanced and sharp local near-field gradients that can result in sufficiently strong optical forces to enable the mechanical manipulation of the proteins [34,109,110]. In the last decade, tremendous advances have been made in designing plasmonic nanostructures that can trap sub-micron particles and larger molecules [111–115]. One of the highly successful plasmonic nanostructures in this regard is the double nanohole (DNH) aperture. In 2012, Gordon’s group demonstrated the trapping of a single molecule of serum albumin (BSA) protein which has a Stokes protein radius of about 3.4 nm. In their experiment they utilized a DNH with each hole size around 200 nm. By measuring the transmission through the DNH they were able to show the trapping of the BSA protein and even observe the transition between two of its protein folding conformations [110]. Using a similar technique, Gordon’s group has also shown that the DNH could detect ligand binding to a single protein. They investigated the interaction for 3 sets of protein interacting with small molecules: biotin−streptavidin, biotin−monovalent streptavidin, and acetylsalicylic acid−cyclooxygenase2 [116]. Furthermore, they also tracked the unzipping of 10 base pair DNA-hairpins, and they quantified how tumor suppressor p53 protein delayed this unzipping process [117]. In addition, they studied the single-molecule protein binding kinetics for a single human serum albumin (HSA) binding to tolbutamide and to phenytoin [118]. Xu et al. introduced fluorescent microscopy that can combine with the DNH plasmonic tweezing to directly track the spatial position of nanoparticles trapped in the DNH [119]. In their work, nanoparticles with a diameter of 20 nm were trapped and observed through a fluorescent microscope. The position distribution of the trapped nanosphere showed an elliptical shape. When higher laser intensity was applied, a tighter spatial confinement of the nanoparticles occurred. To get a clear insight into the trapping process, a comprehensive simulation was performed. They modelled the distributions of the electric field, temperature, fluid velocity, optical force and potential energy. These simulations were combined with simulations of the stochastic Brownian diffusion to predict trajectories of trapped nanoparticles.

Besides being able to directly apply trapping forces to nanoparticles and molecules, plasmonic tweezers can also induce rotational movements of micro/nanoparticles. Huang et. al. [32] used a plasmonic Archimedes spiral structure to generate an optical vortex that could induce orbital rotation for achiral polystyrene microparticles (1 μm diameter). A charge-coupled device (CCD) camera was employed to record the motion of the microspheres. They observed an interesting phenomenon that, depending on the handedness of the input circularly polarized light, the particles experience a force that leads to trapping or a force that leads to rotation. This research in plasmonics enabled the application of forces onto nanoscale particles, therefore it might become possible to manipulate and sort chiral molecules via such optoplasmonic methods.

Despite the rapid development of plasmonic techniques, few of them are associated with plasmonic chiral sorting of nanoscale molecules. As mentioned above, such a device requires a steady trapping potential even for the nanoscale molecules/particles, and the ability to apply handedness dependent forces to molecules/particles. One of the platforms that could potentially fulfil the two requirements above is coaxial nanoaperture [35]. However, the fabrication of such a nanostructure remains a challenge. In 2015, Yoo et al. successfully manufactured this type of resonant plasmonic coaxial nanoaperture with only a 10 nm gap using atomic layer lithography [114]. They showed the capability to trap 30 nm polystyrene nanoparticles and streptavidin

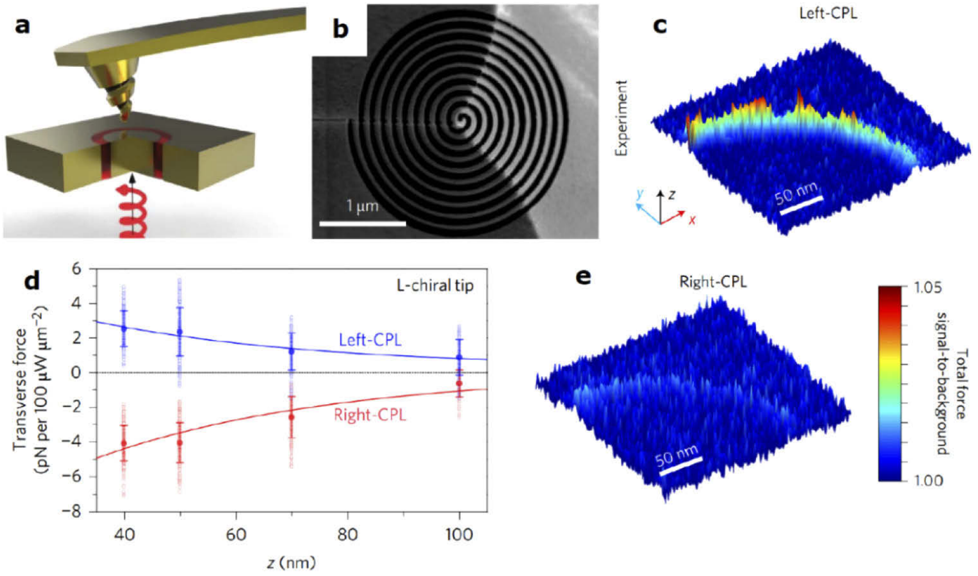

Fig. 8. (a) Schematic illustration of enantioselective force mapping, where CPL illuminates a coaxial nano-aperture made of gold. (b) SEM images of a chiral tip, which is made with focused ion beam milling. Force map on coaxial nano aperture with left (c) and right (e) CPL illumination with ranges indicated in the color bar to the right. (d) Measured transverse forces with the L-chiral tip, with left-handed (blue) and right-handed (red) CPL illumination. Open dots are raw data, filled dots are mean values, and error bars show standard deviations. Reprinted from Ref. [120].

protein molecules with a laser power as low as 4.7 mW. Two years later, Zhao et al. followed up on this theory work and published experiments using the plasmonic coaxial aperture to apply handedness dependent forces [120]. To quantify the optical force, they developed a technique called chiral optical force microscopy and successfully mapped chiral force with 2 nm lateral resolution using atomic force microscopy (AFM). In their work they fabricated a chiral tip for AFM, shown in Figs. 8(a) and (b) to measure the optical force exerted on it. By moving the tip above the coaxial aperture, they were able to measure the force magnitude and direction. Utilizing different CPL illumination and by combining the force measurement with AFM they plotted 1D lateral force map, the result is shown in Fig. 8(d). Based on the 1D lateral force map, a 2D lateral force map can be also plotted, Figs. 8(c) and (e). The experimental results matched with their simulations. For a left-handed chiral tip, transverse forces are observed that are attractive with left-CPL and repulsive with right-CPL. The difference of opposite-handed specimens is larger than 10 pN, which enables both trapping and sorting of small chiral nanoparticles.

4. Synthesis, fabrication, assembly and manipulation of chiral plasmonic nanostructures

Fabrication of 3D chiral nanostructures is of fundamental importance for developing a better understanding of chiroptical sensing and manipulation techniques, and for developing real-world applications for the chiral sensors and spectrometers to leave the laboratory. Particularly, the CD spectra of chiral nanostructures reveal that they are markedly sensitive to changes in geometry. The precise fabrication, robust assembly and controlled manipulation of 3D plasmonic nanosystems is therefore a basic requirement in order to make best use of the plasmon-enhanced chiroptical sensors. Achieving the controlled fabrication, however, remains a key challenge. In the following we review some of the main routes to synthesis, fabrication, assembly and manipulation of chiral plasmonic nanostructures [121–123].

One identifies two basic types of nanofabrication approaches that are available for assembling plasmonic nanosystems, the bottom-up and the top-down fabrication. The top-down fabrication approach applies nanofabrication tools such as electron-beam lithography (EBL) [124], focused-ion beam etching [125], and direct laser writing (DLW) [126] to transfer precise design files into patterns of nanostructures, typically on a planar substrate. Techniques such as EBL allow for the fabrication of nanostructures with a high spatial resolution of about 1.5 nm [127]. The bottom-up assembly approach, on the other hand, exploits the intrinsic properties of atoms and molecules to direct the self-assembly of the nanosystem. The self-assembly can make use of biological building blocks such as DNA, resulting in biocompatible nanostructures [128] that are built with oligonucleotides, longer DNA strands, (parts of) plasmids, and (parts of) viral genomes. Peptide [129] directed self-assembly allows the assembly of nanostructures with a sub-10 nanometer precision [130]; free-floating 3D structures and the assembly of reconfigurable and dynamic nanosystems have been demonstrated with DNA [131].

4.1. Bottom-up, DNA-directed assembly and manipulation of chiral plasmonic nanostructures

Among the variety of materials that have been explored with the bottom-up approach, DNA stands out as the most widely utilized, providing a very high level of programmability of the assembly process via the DNA base-pair interactions [128,132]. Various DNA nanostructures have been assembled for proof-of-principle studies of sensing and manipulation [133–135], and some of them have been used as platforms for molecule detection [136], to study chemical reactions [137] and nanomaterials [138], for the characterization of biomolecular interactions [28] and for the assembly of enzymatic cascades [139] and advanced drug-delivery vehicles [140].

The DNA origami approach, introduced by Seeman [133] and others, relies on the hybridization and the nanoscale folding of a long scaffold DNA strand, with the help of DNA staple strands, into DNA nano-architectures with often complex and arbitrary quasi 2D [133,141–146] and 3D geometries [147–149]. The DNA origami technique offers excellent control over the spatial assembly of nanoscale patterns with typically sub-10 nm precision [130]. DNA origami technology has been used to assemble nanostructures and nanoarrays together with other materials such as proteins [150], gold nanoparticles [151], and mRNAs [141], often including unique biopolymer sequences that define deterministic binding sites for the downstream assembly of molecular and nanoparticle building blocks [147–149,152]. In DNA origami, individual helper strands can be modified with a sequence-dependent surface tag to attach a variety of other materials to the scaffold. For example, DNA origami has been utilized as a template to assemble functionalized metallic and semiconducting nanocrystals, carbon nanotubes and biological materials, into sophisticated geometries and with nanometer precision [138,153–157]. Plasmonic structures consisting of metal nanoparticles made of silver and gold [2] have been arranged into DNA nanostructures that help amplify the weak optical signals of chiral molecules [141,158] and that provide an elegant way for achieving strong optical activity in the visible spectral range [128]. The assembly of the chiral plasmonic structures makes use of the flexibility and programmability offered by DNA-origami with endless possibilities for assembling nanostructures and -systems with remarkable structural complexity and rigidity [20,149,159,160] and with a strong chiroptical response [20,130,161]. The chiroptical structures that are dynamic can be promising candidates for sensing because changes in the structural configuration can be associated with changes in the CD spectra [162]. Already, there are a variety of responsive/reconfigurable dynamic chiral plasmonic nanostructures which are driven by physical or chemical inputs such as toehold-mediated DNA strand displacement reactions [163], change in pH [164], ion concentration [165], application of magnetic fields, and light [166], and with thermal stimuli [165]. Their applications range from adaptable nanophotonic circuitry and optical molecular sensing [167,168] to the control of molecular dynamics [130,138], and carbon nanotube devices and platforms [153].

Li et al. [169] have demonstrated a nanoscale reconfigurable device combining the programmable DNA origami technique with chiral plasmonics. Two gold nanorods 40 nm × 10 nm were attached on the reconfigurable DNA origami platform consisting of two connected bundles of self-assembled DNA strands which subtended a tunable angle, see Fig. 9. The handedness of the 3D chiral nanostructure was controlled by using two DNA locks, which were each made of oligonucleotides extending from the sides of the origami scaffold, and used to lock-in-place one of the configurations of the nanostructure by DNA hybridization, see Fig. 9(a), the four arms of the two DNA locks are labelled a, b, c and d. Through toehold-mediated DNA strand displacement reactions, the plasmonic nanostructure can be driven to either a left- or right-handed state by adding strands R1 or R2, and back to its relaxed state by adding return strands R1 or R2, see Fig. 9(b). This switching process was monitored by CD at a fixed wavelength of 725 nm. As shown in Fig. 9(c), the switching among the three different states, the left-handed and relaxed states by adding R1 in sequence (Fig. 9(c1)) and between the right-handed and relaxed states by adding R2 in sequence (Fig. 9(c3)) was demonstrated in multiple cycles and this required successive additions of so called DNA fuel strands that drive the processes. The red and black curves correspond to the CD spectra of the left-handed and relaxed states in the first cycle of 1, see Fig. 9(c2), and the blue and black curves corresponding to the CD spectra of the right-handed and relaxed states, see Fig. 9(c4). This work is an important example of a reconfigurable chiral structure with fully switchable chirality that which can find use as the dynamic element of a chiral sensor.

In related work, a reconfigurable plasmonic DNA structure has been described in [170]. The handedness was switched by the toehold-mediated DNA strand displacement reaction. Here, AuNRs were assembled into reconfigurable plasmonic diastereomers with up to three distinguishable chiral centers. Each chiral center was selectively controlled to switch between left-handed and right-handed states to generate the desired diastereomers, giving rise to characteristic

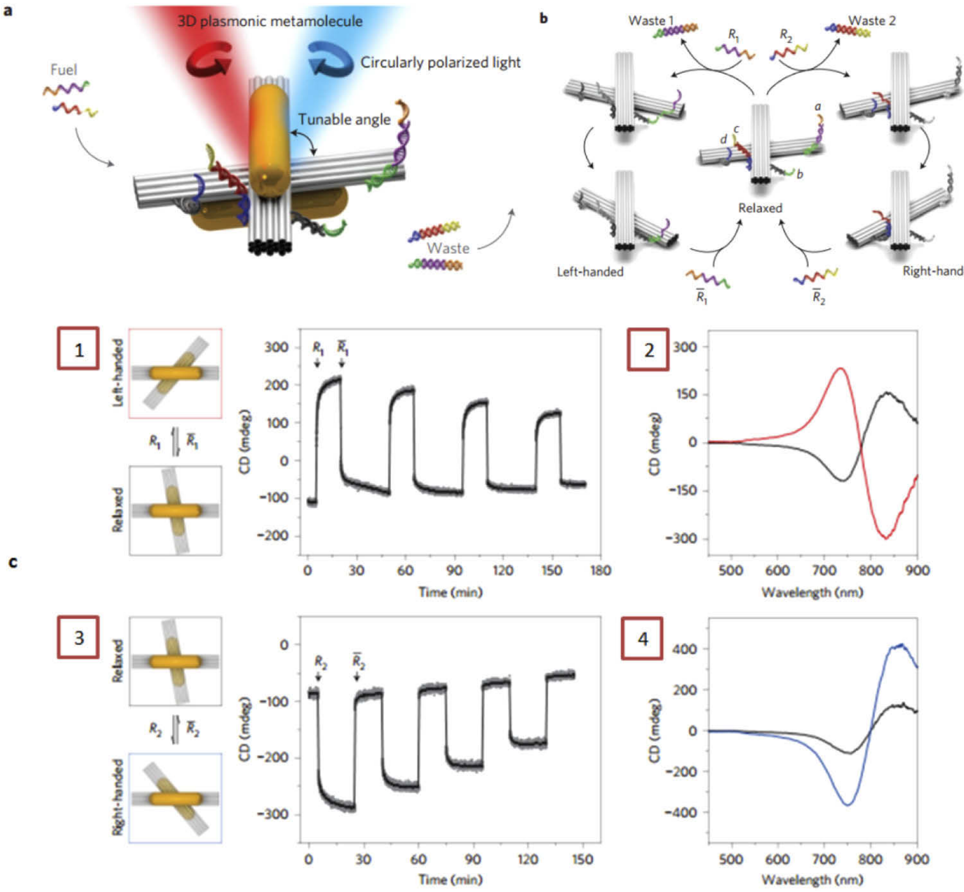

Fig. 9. Design and operation principle; (a) Schematics of the DNA origami-based 3D chiral plasmonic nanostructure, two gold nanorods (AuNRs) are attached onto a switchable DNA origami template consisting of two connected bundles, which subtends a tunable angle. Two AuNRs constitute a three-dimensional chiral plasmonic object with a circular dichroism optical response that is dependent on the angle between the rods. The red and blue beams indicate the incident left-and right-handed circularly polarized light, respectively. (b) Switching mechanisms, the plasmonic nanostructure can be driven to either the left- or right-handed state by adding removal strands R1 or R2 and back to its relaxed state by adding return strands R2 or R1. (c) Switching between the left-handed and relaxed states by adding R1 in sequence (c-1, c-2) or between the right-handed and relaxed states by adding R2 in sequence (c-3, c-4). The related CD signals have been shown in (c-2, c-4) with the red and black curves and blue and black curves, respectively. The right-handed state exhibits much larger CD response than the relaxed state. The relaxed state exhibits a slight right-handed preference. Reprinted with permission, from Ref. [169].

chiroptical CD signals. The DNA origami template consisted of a two-layer rectangular plate and 10-helix bundle linked in the center, with one AuNR attached to the plate and one to the bundle. The relative orientation of the bundle and the plate, and hence of the nanorods, was actively switched between the right- and left-handed chiral configurations using the DNA strand displacement reactions. The near-field coupling in the chiral centers contributed to the overall strong CD signals [171].

Li et al. [132] showed an all-optically controlled dynamic plasmonic system that is waste-free. Different from the dynamic DNA systems previously reported, this one does not require the fuel strands to drive a DNA strand displacement reactions forward. In this study, light was the energy input and the driver for the conformation changes of the plasmonic nanostructure. The light input offered a high spatial and temporal control of the switching process. Most importantly, light delivered a noninvasive control and read-out of an optically active system, allowing for monitoring the switching operation in real time. The dynamic plasmonic nanostructure comprised AuNR assembled on a reconfigurable DNA origami template by integration of a photoresponsive DNA lock, see Fig. 10(a), namely an azobenzene-modified DNA segment [166]. Light can cyclically 'write' and 'erase' the conformational states of the nanostructure through photoisomerization of azobenzene and consequently translate the light-induced molecular motion of azobenzene into reversible plasmonic chiroptical responses which can be read out in situ by CD, see Fig. 10(b). The conformational switching of azobenzene was actuated by UV and visible light illumination, see Fig. 10(c). The molecular changes of the cis-trans isomerization of azobenzene are amplified through the DNA nanostructure and translate into the detectable and reversible signal amplitudes in CD. This plasmonic nanosystem bears the unique features of optical addressability, reversibility and mouldability, all of which are crucial features for developing all-optical molecular devices [132]; they can offer interesting new avenues for manipulating materials at the nanoscale and for building sensors.

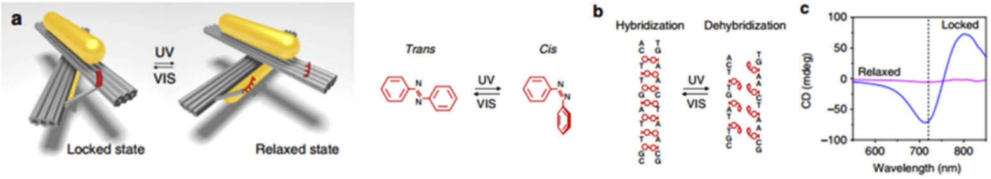

Fig. 10. Light-driven 3D plasmonic nanosystem; (a) schematic of the 3D plasmonic nanosystem regulated by UV and vis light illumination for switching between the locked right-handed and relaxed states, (b) trans–cis photoisomerization of an azobenzene molecule by UV and vis light illumination, hybridization and dehybridization of azobenzene-modified DNA oligonucleotides controlled by trans–cis photoisomerization of azobenzene through UV and vis light illumination, (c) Measured CD spectra after UV (purple) and vis (blue) illumination. Reprinted from Ref. [132].

The selective control of reconfigurable chiral plasmonic metamolecules assembled by DNA origami using pH has been demonstrated in [172] see Fig. 11(a). As shown in Fig. 11(b), a pH-sensitive DNA lock contained a DNA triplex formed through pH-dependent Hoogsteen interactions (dots) that form between ssDNA and a DNA duplex (dashed). The transition pH value of the DNA lock, where the locked and opened states exchange, could be precisely programmed over a wide pH range by varying the relative content of TAT/CGC triplets. The ability to engineer DNA structural dynamics with a programmable pH response opens interesting avenues in sensing.

In living cells, molecular motors such as kinesin and dynein can walk directionally along microtubules to ferry cargoes [173]. Such biological machines were the inspiration for the development of artificial DNA walkers [155,156] and plasmonic walkers [123,159], which were used to demonstrate directional, progressive, and reverse nanoscale walking on DNA

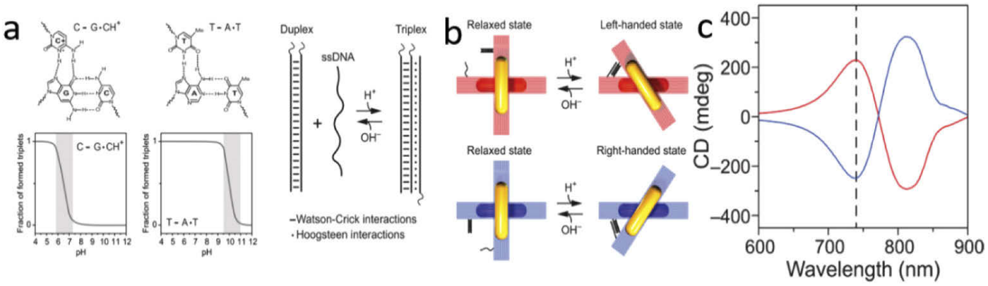

Fig. 11. Working principle of the pH-sensitive plasmonic metamolecules; (a, left side) pH-triggered DNA lock, (a, right side) pH-regulation of the DNA origami–based chiral metamolecules, (b) The metamolecules can be switched between the relaxed and the LH/RH state by opening or closing the pH-triggered DNA locks. (C) Measured CD spectra of the metamolecules in the LH (red line) and the RH (blue line) state from the LH 50% and RH 50% samples at pH 5.5, respectively. Reprinted from Ref. [172].

origami [123,174]. Liu et al. demonstrated an active plasmonic system in which a gold nanorod can perform stepwise walking [122], directionally and progressively, along a DNA origami nanostructure. The walking dynamics were monitored by in situ CD spectroscopy. The key idea behind this experiment was to create a plasmonic system that resolves the discrete walking steps by correlating them to a series of CD signal changes. Structural design of the walker system is shown in Figs. 12(a) and (b). Such a walker comprises an anisotropic AuNR as its 'body' and discrete DNA strands as its 'feet'. The walker, the yellow AuNR in Fig. 12(a), walks along the direction of the long axis of a second red AuNR (called stator) that is located on the opposite side of the planar DNA origami structure. Changes in the chiral geometry of the two AuNRs result in chiroptical signal changes that are observed for each of the five 'stations 'of the walker, see Figs. 12(a) and (b). When excited by left and right CPL, the plasmons generated in the walkers and the stator are coupled through near-field electromagnetic interactions [159] which contribute to the CD signal changes [122] which are overly sensitive to the configuration changes of the 3D system [175]. The measured CD spectra at each walking station are shown in Fig. 12(c). This work [122] together with [159] suggest a new generation of artificial synthetic machines and sensors, which can report in situ about their own structural dynamics using a noninvasive, robust, and all-optical approach.

4.2. Top-down fabrication of chiral plasmonic nanostructures

The chiral structures fabricated by the bottom-up approach often have only small chiroptical effects in the visible range [176,177]. In quantitative terms of the CD factor, the top-down approach is more successful. There are several tools for the top-down approach such as EBL [124], FIB [178] and DLW [179]. They have been used to fabricate quasi 2D and 3D chiral plasmonic structures [180]. The drawbacks of the top-down approaches are that they often suffer from a high cost, they can be time-consuming; and they often demand complex procedures, a precise alignment of the optical and electron beams, and sometimes the application of many lithographic and deposition steps in sequence. Because of their precise fabrication capabilities, the top-down methods can be used to fabricate plasmonic nanostructures with large CD signals at visible frequencies [125,181]. For example, a new plasmonic metamaterial array with a theoretical CD of over 50% over a bandwidth of 100 nm has been designed and fabricated by EBL [181]. The planar geometry helped to simplify the top-down fabrication processes. In another example, the FIB technique has been used to fabricate two-dimensional (2D) periodic arrays of 3D plasmonic ramp-shaped nanostructures that exhibited large CD up to 64% in the

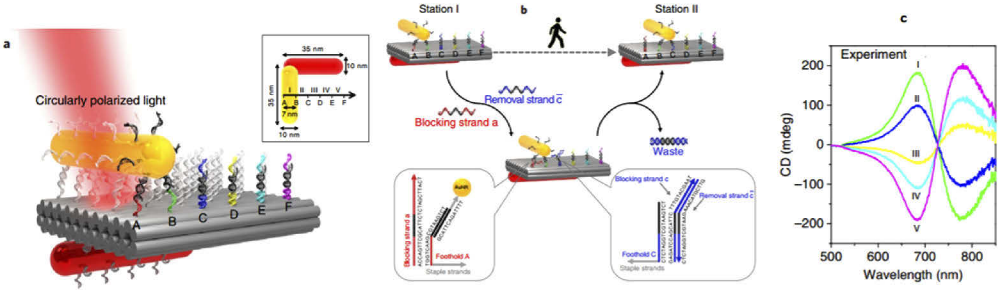

Fig. 12. Schematic of the plasmonic walker; (a) two gold nanorods (AuNRs) are assembled perpendicularly to one another on a double-layer DNA origami template, forming a left-handed configuration at station I. The yellow AuNR on the top surface represents the 'walker' and the red AuNR on the bottom surface represents the 'stator'. The walking track comprises six rows of footholds (A–F) extended from the origami surface to define five walking stations (I–V). The walker AuNR is fully functionalized with foot strands. To enable robust binding, the walker steps on two rows of neighboring footholds at each station. The red beam indicates the incident circularly polarized light, (b, c) walking mechanism, measured CD spectra at each station. Initially, the walker resides at station I. On addition of blocking strand a, and removal of strand c, two toehold-mediated strand-displacement reactions occur simultaneously. Blocking strand a triggers the dissociation of the walker's feet from footholds A. Row A is then site-blocked. Meanwhile, removal strand c releases blocking strand c from footholds C. Row C is therefore site activated to bind the feet of the walker. Subsequently, the walker carries out one step forward, reaching station B. Reprinted from Ref. [122].

visible range [125]. In another example, nanohelices were fabricated by two-photon DLW [182] and those have been used as broadband circular polarizers with high CD in the mid-IR [27].

4.2.1. Top-down fabrication of chiral (plasmonic) nanostructures by direct laser writing

Three-dimensional chiral photonic superlattices composed of different checkerboard-like arrangements of polymer spirals fabricated by DLW have been investigated in [183]. Chiral optical properties strongly depended on the relative phase shift and handedness of the spirals, generating different CD resonances. Cubic unit cells composed of four spirals with lattice constant a, and with the same structural features but with a varying phase have been fabricated by direct-laser writing, see Fig. 13(a), using the negative-tone photoresist SU-8. The full opening angle of the incident light impinging under normal incidence was reduced to about 5° to avoid smearing out sharp spectral features. Four spirals with the same handedness were laterally arranged in sample I, see Fig. 13(a). The phase of the spirals of sample II and III have been shifted, and sample IV is the racemic mixture state. The measured optical transmittance spectra of the samples I-IV taken under normal incidence for circular polarization of the incident light, are shown in Fig. 13(c). They show a polarization stop band for sample I centered at 4.3 um [184]. The optical properties of samples I–III are similar. In contrast, the stop band disappears for sample IV. For the samples II and III, a second additional set of longer-wavelength resonances were observed. Furthermore, for sample III, the original polarization stop band has been strongly suppressed, whereas it is still visible in sample II. Finally, the racemic mixture sample IV hardly shows any chiral response. Nevertheless, the longer wavelength stop band also seen for samples II and III is still present. The chiral optical properties strongly depend on the in-plane arrangement of the spirals rather than solely on the spiral parameters. This opens new design options for tailoring the optical properties of these artificial chiral structures that could be applied to plasmonic systems.

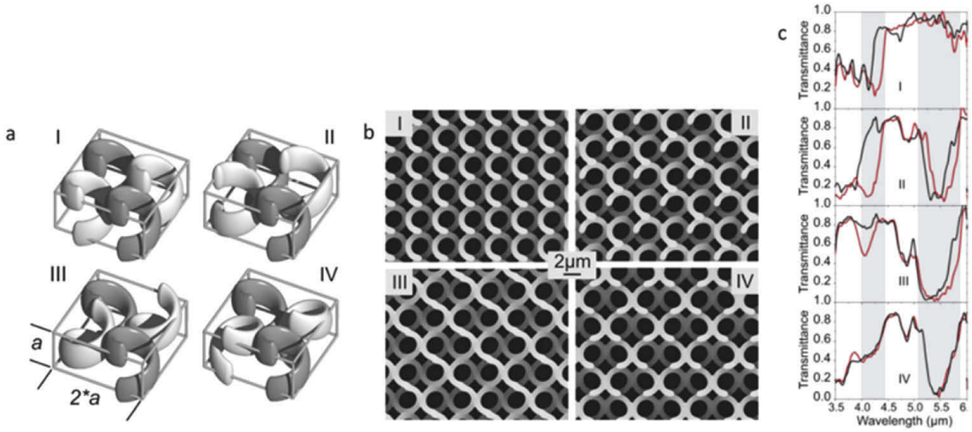

Fig. 13. (a) Four configurations of chiral photonic crystals: Spirals with the same handedness are in phase (I), 90° out of phase (II), and 180° out of phase (III). (b) Top-view electron micrographs of fabricated circular-spiral photonic crystals. (c) Transmittance spectra of the four different samples (I-IV) under circular polarization of the incident light, black and red curves for left- and right-handed, respectively. The gray areas highlight stop bands for circular polarization or polarization-independent stop band. Reprinted from Ref. [183].

Other work by Gansel et al. [185] utilized the DLW technique for fabrication of chiral metamaterial helices. In this work, tapered gold-helix metamaterials were fabricated with the help of DLW followed by electroplating, to broaden the operation bandwidth of their devices in the THz region and to improve extinction ratios. The measured extinction ratio for CPL exceeded 10 throughout the entire operation bandwidth. According to numerical calculation, it has been shown that the bandwidth could be increased to span 1.5 octaves by tapering the gold-helix radius. The structure can be useful as a polarizer or as an analyzer, depending on the side from which light impinges onto the tapered helices.

4.2.2. Top-down fabrication of chiral plasmonic nanostructures by focused ion beam

In 2014, Marco et al. published their work on fabrication and characterization of chiral metallic nanospirals in the visible and near infrared range [186]. In this work they employed the FIB induced deposition (FIBID) technique. The precursor metal-organic compounds are decomposed by an ion beam and absorbed onto the substrate. The handedness of the nanospirals is controlled by sweeping the ion beam in a clockwise or counterclockwise direction. The growth and evolution of nanostructures are influenced by the effect of the surface charge, which induces a gradient in the spiral structure. One year later, the same group demonstrated the fabrication of intertwined, triple-helical nanowires structures using tomographic rotary growth [187]. Rotational symmetry, intrinsically lacking in helix geometry, can be effectively restored with a packed multi-helices arrangement in a single cell. By packing multiple-helices in a single cell, the cross-polarization conversion from anisotropy is eliminated. These triple- helical nanowires show up to 37% of CD in a broad range from 500–1000 nm, see Fig. 14(a).

In terms of plasmonic metasurfaces, a simple technique to fabricate such structures is FIB milling. Highly focused ion beams such as Ga+ are used to locally sputter or mill a sample surface inside a vacuum chamber. This technique produces only minor changes to the optical responses of metals. A schematic fabrication example is shown in Fig. 14(b). Mohsen et al. proposed a planar array of plasmonic ramp-shaped nanostructures [125]. The structure is fabricated on a gold evaporated glass slide. Optical experimental characterization can be performed for negative ramp-shaped structures. CD is measured when illuminated by CPL with corresponding unit cell

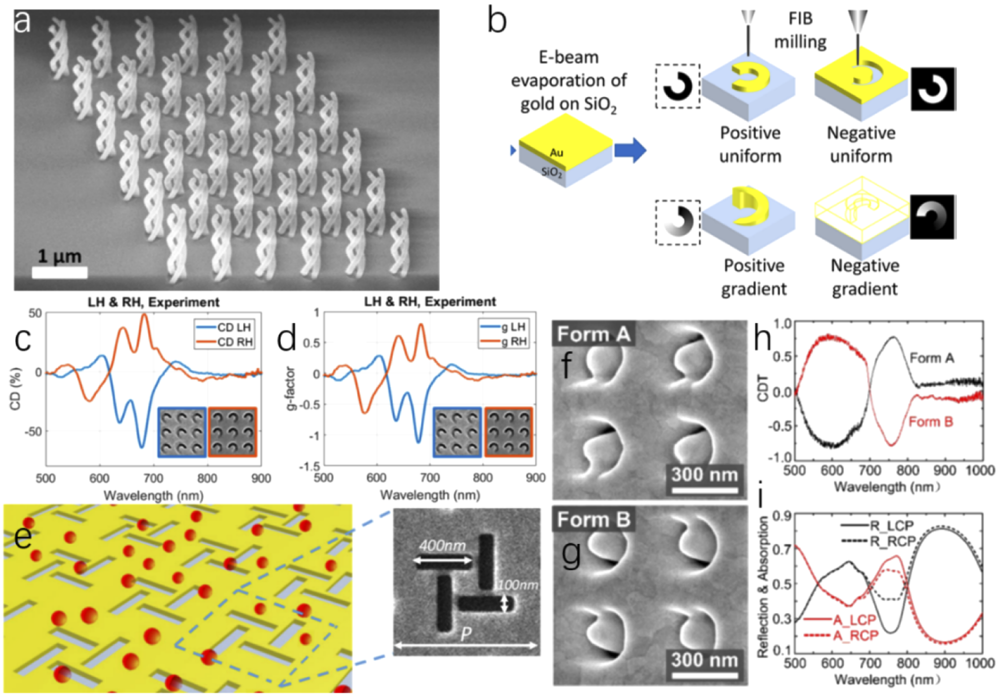

Fig. 14. (a) SEM view of multiple wire helix array realized by focused ion beam-induced deposition. Reprinted from Ref. [189]. (b) Fabrication procedure of uniform/gradient and positive/negative variants of the ramp-shaped nanostructure. (c, d) Comparison between the measured CDs and g- factor obtained from the LH and the RH structures. Reprinted from Ref. [125]. (e) Left: Schematic illustration of the hybrid system in which the red dots represent CQDs and the yellow film with slits is the chiral metasurface. Right: SEM image of the left-handed chiral unit cell. Reprinted from Ref. [188]. (f, g) SEM images of the fabricated chiral metamaterials in Form A and Form B with a slant angle of 40° (h) Measured CDT spectra of the two forms of metamaterials. (i) measured reflection spectra (R_LCP and R_RCP) and absorption spectra (A_LCP and A_RCP) for Form A under LCP and RCP illumination. Reprinted from Ref. [190].

shown in the SEM image in the inset of Figs. 14(c) and (d). The reflection spectrum shows a CD as high as 64% and a dissymmetry factor of 1.13 at 678 nm (shown in Figs. 14(c) and (d)). Zeng et al. reported the chiral functionalization of achiral CdSe/ZnS core-shell quantum dots (CQDs) [188]. They designed plasmonic chiral metasurfaces as shown in Fig. 14(e), and by combining the response of CQDs and tunable chiral metasurfaces, induced chiral features arise with correlation to the absorption bands of CQDs and the chiral bands of the metasurfaces. This structure is fabricated using an FIB milling process on a 100 nm thick gold film. Characterization of CD transmission spectra for both left and right-handed CPL is performed, then compared for with and without CQDs. A clear CD signal enhancement was observed.

Yang et al. proposed a design for chiral plasmonic metamaterials based on plasmonic slanted nanoapertures [190]. These structures are fabricated by tilting the sample substrate relative to the FIB, by the angle between the sample surface normal and the incident direction of the ion beam. Therefore, highly uniform slanted nanoapertures with arbitrary shapes can be molded. Figures 14(f) and (g) shows the SEM images of two forms of structures with a slanted angle of 40 °. They are mirror images with different handedness, named form A and form B (see Figs. 14(f) and (g)). Transmission along the nanoapertures is determined by the strong plasmonic enantioselective chiral near-field. Which means the apertures enable more passage of one handedness CPL while reflecting the other one, this phenomenon originates from the coupling process of CD mode in the slanted nanoapertures, which is induced by the spin –dependent field overlap. Figure 14(h) shows their measured CD in transmission (CDT) for both forms of aperture, where form A exhibits an opposite behavior to form B. The same phenomenon is also observed in the reflection and absorption measurements. These findings could be applied in the field of biosensing, where absorbed chiral molecules may change the transmission through the aperture according to their handedness.

4.2.3. Top-down fabrication of chiral plasmonic nanostructures by electron beam lithography

A 3D chiral plasmonic structure has been fabricated with one step EBL in [124]. The 3D plasmonic chiral structure comprised aligned L-shape and disk-shape gold nanostructures on the two sides of a suspended ultrathin silicon nitride (Si_3N_4) membrane. L-shape gold nanostructures are at the bottom surface of Si_3N_4 membrane, and the disk-shaped ones are on the top surface. The L-shape gold nanostructures are arranged on a plane into an L-shape nanostructure without changing the C_4 symmetry. The L-shape nanostructure has a dimension of 200 nm in width and 400 nm in length as shown in Fig. 15(a).

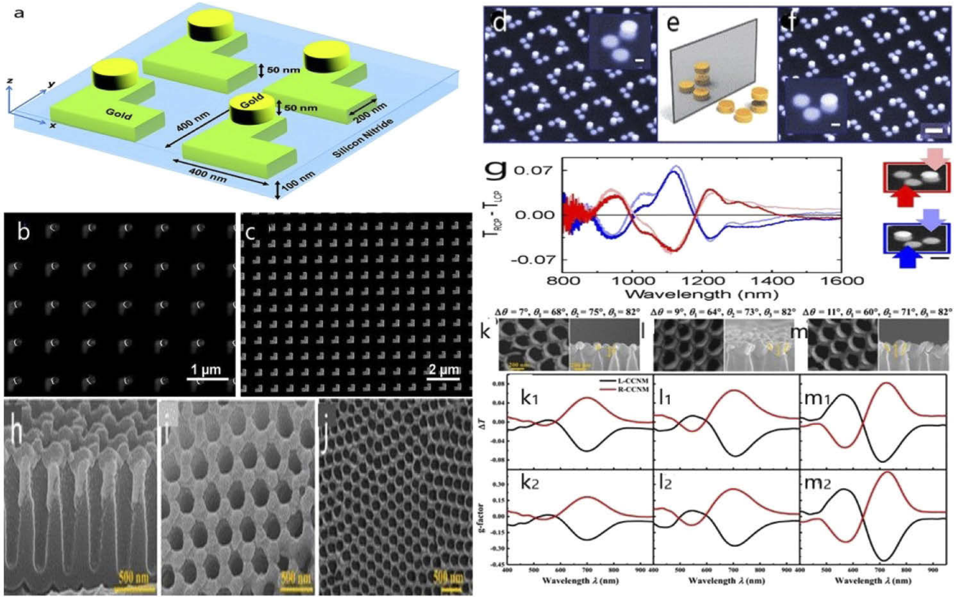

Fig. 15. (a) Schematic of the L – disk plasmonic chiral nanostructures. SEM images of the 3D gold nanostructures (b) top-view of the disk-array and (c) bottom-view of the L-array. Reprinted from Ref. [124] (d,f) SEM images of the chiral plasmonic molecules in a tilted overview. The scale bar of the overview is 500 nm and inset is 100 nm. (e) Schematic sketch of the chiral plasmonic molecules (g) Difference in transmittance of right – and left-handed CPL obtained by varying the relative position of the upper dots of the plasmonic structures illuminating from opposite directions. Reprinted from Ref. [191] (h) the tilting-view of the SEM image of the R-CCNM on the AAO template (i) the top-view of the SEM images of R-CCNM on AAO template and (j) on Si substrate. (k,l,m) The top view (on Si template) and bottom view (on AAO template) SEM images of R-CCNM in left and right columns with varying incident angles. (k_1, l_1, m_1) ΔT and (k_2, l_2, m_2) g-factor spectra obtained for the L-CCNM and R-CCNM with relevant incident angles. Reprinted from Ref. [192].

The suspended membrane plays a key role by facilitating an ultra-smooth interface and the uniformly controlled ultra-small separation of the top and bottom layers of the nanostructure. SEM images of the suspended 3D gold nanostructures are shown in Fig. 15(b) (top view of the disk array) and in Fig. 15(c) (bottom view of L array). The unique contrast in the sensitivity of the selected resists polymethyl methacrylate (PMMA) and ZEP (ZEON resist) enables separated exposure doses of electron beams to pattern the top and bottom surfaces. No alignment steps are involved when using this technique. The 3D patterns can be designed and created in single-step EBL.

Three-dimensional plasmonic oligomers, shown in Fig. 15(e), can form artificial plasmonic molecules showing strong chiroptical response [191]. The oligomers are composed of individual metallic nanoparticles and the properties can be arbitrarily changed. The authors reported that the plasmon resonance from the near-field coupling is the reason behind the chiroptical response. These clusters of nanoparticles are fabricated with top-down EBL techniques combined with layer-by-layer stacking and are spectrally highly tunable. The two-layer quadrumer structures are fabricated with three particles arranged in an L-shape in the first layer and the fourth particle (a single dot) stacked on-top of first layer, as shown in Fig. 15(e). The tilted overview of the SEM images of the plasmonic structures are shown in Fig. 15(d) and in Fig. 15(f). The position of the single dot determines the handedness of the structure. ΔT is defined as the difference in transmittance T_{RCP} and T_{LCP} for right- and left-handed CPL, respectively. Changing the handedness of the structure by varying the relative position of the single dot, the ΔT spectra can be flipped as shown in Fig. 15(g). Similar spectra are obtained for illuminating the oligomers from opposite directions and the handedness does not depend on the direction of propagation of light. Fabricating a series of clusters by displacing the fourth particle (on top of first layer) from the symmetric position of the achiral structure, the chiral plasmonic cluster can function as a 3D chiral plasmon ruler with strongly modulated optical spectra. The authors suggest that these clusters of nanoparticles are expected to show a strong response and coupling with chiral biomolecules to possibly enable chiral sensing with a high sensitivity.

A method for preparing plasmonic chiral nanostructures (PCN) showing strong chiroptical response and enhanced near-fields, enabling a sensitive biomolecule detection has been demonstrated in [192]. The PCN is a chiral conic nanoshell metallic nanostructure (CCNM) generated on an achiral tapered nanopore anodic aluminum oxide template (AAO). The CCNM consists of three nanoshells of different heights generated by varying the incidence and orientation angles of deposition. CCNM couples the incident light into the nanostructure and confines the electromagnetic energy inside the shell. EBL has been used for fabricating PCN. Due to the low speed of operation and high cost of EBL, it may be replaced by Glancing angle deposition (GLAD), a low-cost technique with a geometric shadowing effect. In this technique, a periodic nanocone array is constructed on an AAO template. Chiral nanoshells are generated with a three-step deposition of Ag vapor with different azimuthal and oblique angles. Later, the substrate is rotated clockwise or anticlockwise to fabricate right (R-) and left-handed (L-) CCNMS. SEM images of R - CCNM are shown in Figs. 15(h)-(j). The ΔT response and g-factor spectra of the L- CCNM and R-CCNM can be altered by varying incident angles as shown Figs. 15(k_1), (l_1), and (m_1)) and Figs. 13(k_2), (l_2), and (m_2) respectively. CD responses are obtained by tuning the incidence and orientation angles of the deposition and the template parameter. The chirality enhancement of CCNM shows distinct interaction with biomolecules resulting in an asymmetry in the optical characteristics of R- and L- CCNMS. This enables CCNM detection and analysis of chiral features of chiral molecules. The authors reported chiral signals were enhanced by two orders of magnitude while detecting chiral molecules with CCNM.

4.3. Other types of fabrication: core-shell plasmonic nanostructures

In [193], the metallic helix array of 3D core-shell architecture enhances the sensing properties of the chiral metamaterial in the far- and the near-field. In this structure, the single right-handed platinum helix, as a core, has been covered with an ultrathin dielectric polymeric shell. Experimental results indicate a spectral redshift of the CD bands in the vis region after the shell deposition, which is related to the enhancement of the refractive index around the nanostructure. The measurements of scattering spectra demonstrate that the core-shell architecture shows a strong enhancement of the far-field scattering, by a factor of 0.8 for RCP and 2,7 for LCP with respect to the bare metallic helix. Furthermore, numerical analysis of the near-field distribution for both bare and core-shell nanostructures state an enhancement in intensity after shell coating. Therefore, the resulting core-shell architecture offers not only an ideal surface coverage for high stability molecular immobilization onto the nanohelices, but also enhances the near-and far-field scattering of the nanohelices for potential sensing applications.

The Core-shell nanosystems are expected to modify the electric field distribution around the nanostructures.In [194], the great importance of close gap nanoparticle dimers has been highlighted because of dramatic electromagnetic field confinement and enhancement in the hot spot. In this study, the aluminum (Al), as a core, and Al oxide shell, naturally occurring when Al nanostructures are exposed to the ambient air, are used to fabricate Al bowtie dimers as a nanoplasmonic-based device with close gaps down to 3 nm. In this structure, the thickness of Al oxide layer is of a few nm, which result in much closer nanogaps between tips of dimers, suggesting Al oxide growth on the pure Al outer surface. Ultranarrow gap bowtie nanoantennas highlight the possibility of enhanced light scattering operating in the UV/vis spectral region.

5. Discussion

Research on the plasmon enhancements of the chiroptical response of molecules and nanostructures is advancing rapidly. Many of the detection systems that we have reviewed exhibit detection limits that are relevant in health and environmental sensing. With the advent of top-down and bottom-up fabrication methods for (chiral) plasmonic nanostructures, further advances in improving existing high sensitivities and selectivity will be possible. Fabricating precise plasmonic nanostructures, with sub-nm precision using top-down methods for the plasmon-enhanced sensing of chiral molecules is a particularly promising approach because it enables on-chip sensing applications. In ultra-sensitive detection, further advances remain possible by reading out the chiroptical response with extremely sensitive techniques that can move beyond the detection limits of CD, ORD and VROA. One example for this is the readout of the optical response of plasmonic nanostructures with interferometers, and optical microcavities in particular [9,12,13]. Applying microcavity-based optical precision measurements [13] to chiral sensing can aid the quest of achieving an ultimate sensitivity at the level of single chiral molecules, of separating the enantiomers, and of establishing control-loops that provide real-time input to chiroptical nanosystems and chiral molecular machines.

The well controlled experimental schemes that are emerging for sensing and manipulating chiral molecules and nanostructures benefit from the ever-improving precision of top-down fabrication methods. The bottom-up assembly of chiral nanosystems, although less precise, is appealing for assembly of dynamic nanostructures that respond to light, or molecules, and that can act synchronously in response to physical and chemical inputs. In some examples such responses are visible to the naked eye and this allows for low-cost sensing applications. Investigating the interactions of chiral molecules with complex (chiral) plasmonic nanostructures will bolster our theoretical understanding and the development of a more complete and predictive theoretical capacity in chiral and complex photonics. Emerging capabilities for precise localization of chiral molecules [11] together with the precise control of plasmonic near-fields can enable further advances in the ultra-sensitive detection and manipulation of enantiomers, especially where maximizing the chiroptical response requires single-molecule localization and alignment with respect to the local electromagnetic vector fields. One may also speculate about further advances in the control of the enantioselective synthesis with light. To investigate chiroptical chemical synthesis mechanisms, the nanoscale positioning of molecules, ultra-sensitive single-molecule sensing and the precise control of near-fields on precisely fabricated and aligned plasmonic nanostructures are the enabling capabilities that need to come together. Methods for optical trapping of molecules combined with ultra-sensitive single-molecule detection may enable experiments that can directly apply and measure the very weak chiroptical forces acting on molecules, and in the presence of Brownian motion. Further advances of LSPR-based single-molecule sensors can enable observation and applications of chiroptical molecular switches [195]. With the help of plasmonic enhancement, the weak lateral chiral force may be boosted at a level where they reveal a distinct effect on the enantiomers and thereby provide an approach towards the optically passive sorting of chiral molecules.

Chirality lays the foundation for many natural phenomena. Chiral molecules play a significant role in many biological and chemical processes. These roles have been elucidated by the detecting and sensing of chiral biomolecules with established methods including fluorescence spectroscopy, colorimetric techniques, CD and other chiroptical methods such as VROA and ORD. This review shows that sensing chiral molecules with plasmonic nanostructures and leveraging their near-field enhancements can be more efficacious in getting strong chiroptical signals. Fortunately, suitable plasmonic nanostructures are becoming more widely available due to the advent of bottom-up and top-down fabrication techniques, as research tools for biosensing, down to single molecules. Plasmonic dimers and DNH already offer the possibility of detecting large biomolecules like proteins and enzymes.

In this review, the application of plasmonics in the field of chiral biosensors has been discussed. Great challenges remain for the chiral biosensing of molecular enantiomers. We need to develop more effective enantioselective selectors and highly sensitive, portable biosensor probes. The combination of the concepts of LSPR and microfluidic systems will aid the development of biosensing assays that operate on a chip and at a low-cost. The insights gained from the LSPR studies can inform the research on SPR platforms which thus far have only shown chiral sensing in bulk measurement and with low efficiencies [196]; no single molecule study has been reported for SPR due to the low sensitivity of the current approaches, to best of our knowledge. Applying new ideas from LSPR sensing to SPR can perhaps break the deadlock. SPR is a widely used technique and advancing its chiral sensing capabilities with LSPR and other methods would be important. Examples for other methods are whispering-gallery mode LSPR/SPR (optoplasmonic) sensors which could provide unparalleled sensitivity for single-molecule chiral sensing.

Funding. Royal Society (Wolfson Research Merit Award); European Research Council (ULTRACHIRAL, ID: 737071); Engineering and Physical Sciences Research Council; EPSRC Centre for Doctoral Training (CDT) in Metamaterials (XM2).

Acknowledgments. The authors acknowledge funding from the University of Exeter, the EPSRC Centre for Doctoral Training (CDT) in Metamaterials (XM^2), the Engineering and Physical Sciences Research Council (Ref. EP/R031428/1), and from the European Research Council under an H2020-FET open grant (ULTRACHIRAL, ID: 737071), as well as funding from The Royal Society (Wolfson Research Merit Award to FV). The authors thank Gillian Fearnyough for proofreading the manuscript.

Disclosures. The authors declare no conflicts of interest.

Data availability. No data were generated or analyzed in the presented research.

References

1. K. Saha, S. S. Agasti, C. Kim, X. Li, and V. M. Rotello, "Gold nanoparticles in chemical and biological sensing," Chem. Rev. **112**(5), 2739–2779 (2012).
2. S. J. Tan, M. J. Campolongo, D. Luo, and W. Cheng, "Building plasmonic nanostructures with DNA," Nat. Nanotechnol. **6**(5), 268–276 (2011).

3. M. M. Miller and A. A. Lazarides, "Sensitivity of metal nanoparticle surface plasmon resonance to the dielectric environment," J. Phys. Chem. B **109**(46), 21556–21565 (2005).
4. H. H. Jeong, A. G. Mark, M. Alarcon-Correa, I. Kim, P. Oswald, T. C. Lee, and P. Fischer, "Dispersion and shape engineered plasmonic nanosensors," Nat. Commun. **7**(1), 11331 (2016).
5. S. Unser, I. Bruzas, J. He, and L. Sagle, "Localized Surface Plasmon Resonance Biosensing: Current Challenges and Approaches," Sensors **15**(7), 15684–15716 (2015).
6. J. Xavier, S. Vincent, F. Meder, and F. Vollmer, "Advances in optoplasmonic sensors–combining optical nano/microcavities and photonic crystals with plasmonic nanostructures and nanoparticles," Nanophotonics **7**(1), 1–38 (2018).
7. P. M. R. Paulo, P. Zijlstra, M. Orrit, E. Garcia-Fernandez, T. C. S. Pace, A. S. Viana, and S. M. B. Costa, "Tip-Specific Functionalization of Gold Nanorods for Plasmonic Biosensing: Effect of Linker Chain Length," Langmuir **33**(26), 6503–6510 (2017).
8. S. Khatua, P. M. Paulo, H. Yuan, A. Gupta, P. Zijlstra, and M. Orrit, "Resonant plasmonic enhancement of single-molecule fluorescence by individual gold nanorods," ACS Nano **8**(5), 4440–4449 (2014).
9. S. Subramanian, H. Y. Wu, T. Constant, J. Xavier, and F. Vollmer, "Label-Free Optical Single-Molecule Micro- and Nanosensors," Adv. Mater. **30**, 1801246 (2018).
10. S. Celiksoy, W. Ye, K. Wandner, F. Schlapp, K. Kaefer, R. Ahijado-Guzmán, and C. Sönnichsen, "Plasmonic Nanosensors for the Label-free Imaging of Dynamic Protein Patterns," The Journal of Physical Chemistry Letters (2020).
11. S. Vincent, S. Subramanian, and F. Vollmer, "Optoplasmonic characterisation of reversible disulfide interactions at single thiol sites in the attomolar regime," Nat. Commun. **11**(1), 1–8 (2020).
12. M. D. Baaske and F. Vollmer, "Optical observation of single atomic ions interacting with plasmonic nanorods in aqueous solution," Nat. Photonics **10**(11), 733–739 (2016).
13. F. Vollmer and Y. Deshui, "*Optical Whispering Gallery Modes for Biosensing*," (Springer, 2020).
14. D. A. Flockhart and H. S. Nelson, "Single isomer versus racemate: is there a difference? Clinical comparisons in allergy and gastroenterology," CNS Spectr. **7**(S1), 23–27 (2002).
15. J. L. Hammond, N. Bhalla, S. D. Rafiee, and P. Estrela, "Localized surface plasmon resonance as a biosensing platform for developing countries," Biosensors **4**(2), 172–188 (2014).
16. K. M. Mayer and J. H. Hafner, "Localized surface plasmon resonance sensors," Chem. Rev. **111**(6), 3828–3857 (2011).
17. S. Simoncelli, Y. Li, E. Cortés, and S. A. Maier, "Nanoscale control of molecular self-assembly induced by plasmonic hot-electron dynamics," ACS Nano **12**(3), 2184–2192 (2018).
18. S. M. Kim, S. W. Lee, S. Y. Moon, and J. Y. Park, "The effect of hot electrons and surface plasmons on heterogeneous catalysis," J. Phys.: Condens. Matter **28**(25), 254002 (2016).
19. E. Minutella, F. Schulz, and H. Lange, "Excitation-dependence of plasmon-induced hot electrons in gold nanoparticles," J. Phys. Chem. Lett. **8**(19), 4925–4929 (2017).
20. M. Hentschel, M. Schaferling, X. Duan, H. Giessen, and N. Liu, "Chiral plasmonics," Sci. Adv. **3**(5), e1602735 (2017).
21. K. Kim and S. Lee, "Detailed balance analysis of plasmonic metamaterial perovskite solar cells," Opt. Express **27**(16), A1241–A1260 (2019).
22. Y. Y. Lee, R. M. Kim, S. W. Im, M. Balamurugan, and K. T. Nam, "Plasmonic metamaterials for chiral sensing applications," Nanoscale **12**(1), 58–66 (2020).
23. V. E. Bochenkov and T. I. Shabatina, "Chiral Plasmonic Biosensors," Biosensors (Basel) 8(2018).
24. S. Yoo and Q.-H. Park, "Chiral light-matter interaction in optical resonators," Phys. Rev. Lett. **114**(20), 203003 (2015).
25. B. M. Maoz, Y. Chaikin, A. B. Tesler, O. Bar Elli, Z. Fan, A. O. Govorov, and G. Markovich, "Amplification of chiroptical activity of chiral biomolecules by surface plasmons," Nano Lett. **13**(3), 1203–1209 (2013).
26. A. O. Govorov, Z. Fan, P. Hernandez, J. M. Slocik, and R. R. Naik, "Theory of circular dichroism of nanomaterials comprising chiral molecules and nanocrystals: plasmon enhancement, dipole interactions, and dielectric effects," Nano Lett. **10**(4), 1374–1382 (2010).
27. W. Ma, L. Xu, A. F. de Moura, X. Wu, H. Kuang, C. Xu, and N. A. Kotov, "Chiral Inorganic Nanostructures," Chem. Rev. **117**(12), 8041–8093 (2017).
28. E. Hendry, T. Carpy, J. Johnston, M. Popland, R. V. Mikhaylovskiy, A. J. Lapthorn, S. M. Kelly, L. D. Barron, N. Gadegaard, and M. Kadodwala, "Ultrasensitive detection and characterization of biomolecules using superchiral fields," Nat. Nanotechnol. **5**(11), 783–787 (2010).
29. N. Shukla, M. A. Bartel, and A. J. Gellman, "Enantioselective separation on chiral Au nanoparticles," J. Am. Chem. Soc. **132**(25), 8575–8580 (2010).
30. S. Chen, F. Zeuner, M. Weismann, B. Reineke, G. Li, V. K. Valev, K. W. Cheah, N. C. Panoiu, T. Zentgraf, and S. Zhang, "Giant Nonlinear Optical Activity of Achiral Origin in Planar Metasurfaces with Quadratic and Cubic Nonlinearities," Adv. Mater. **28**(15), 2992–2999 (2016).
31. T. Shoji and Y. Tsuboi, "Plasmonic Optical Tweezers toward Molecular Manipulation: Tailoring Plasmonic Nanostructure, Light Source, and Resonant Trapping," J. Phys. Chem. Lett. **5**(17), 2957–2967 (2014).

32. W. Y. Tsai, J. S. Huang, and C. B. Huang, "Selective trapping or rotation of isotropic dielectric microparticles by optical near field in a plasmonic archimedes spiral," Nano Lett. **14**(2), 547–552 (2014).
33. R. Gordon, "Biosensing with nanoaperture optical tweezers," Opt. Laser Technol. **109**, 328–335 (2019).
34. T. Shoji, J. Saitoh, N. Kitamura, F. Nagasawa, K. Murakoshi, H. Yamauchi, S. Ito, H. Miyasaka, H. Ishihara, and Y. Tsuboi, "Permanent fixing or reversible trapping and release of DNA micropatterns on a gold nanostructure using continuous-wave or femtosecond-pulsed near-infrared laser light," J. Am. Chem. Soc. **135**(17), 6643–6648 (2013).
35. Y. Zhao, A. A. Saleh, and J. A. Dionne, "Enantioselective optical trapping of chiral nanoparticles with plasmonic tweezers," ACS Photonics **3**(3), 304–309 (2016).
36. M. Schäferling, "Chirality in Nature and Science," in *Chiral nanophotonics* (Springer, 2017), pp. 5–42.
37. W. T. Kelvin, *Baltimore lectures on molecular dynamics and the wave theory of light* (C.J. Clay and Sons; Publication agency of the Johns Hopkins University, London, Baltimore, 1904), pp. xxi, [1], 703 p.
38. A. Singh, N. Kaur, and H. Kumar Chopra, "Chiral Recognition Methods in Analytical Chemistry: Role of the Chiral Ionic Liquids," Crit. Rev. Anal. Chem. **49**(6), 553–569 (2019).
39. V. Y. Gus'kov, D. A. Sukhareva, I. V. Arslanova, and D. E. Musabirov, "Gas-chromatographic separation of enantiomers of 2-chlorobutane and 2-bromobutane on a cyanuric acid-modified Carboblack C adsorbent," J. Anal. Chem. **72**(10), 1089–1094 (2017).
40. C. Hao, L. Xu, H. Kuang, and C. Xu, "Artificial Chiral Probes and Bioapplications," Advanced Materials (2019).
41. W. A. Paiva-Marques, F. Reyes Gomez, O. N. Oliveira Jr., and J. R. Mejia-Salazar, "Chiral Plasmonics and Their Potential for Point-of-Care Biosensing Applications," Sensors (Basel) 20(2020).
42. E. Zor, H. Bingol, and M. Ersoz, "Chiral sensors," TrAC Trends in Analytical Chemistry 121(2019).
43. K. Ngamdee and W. Ngeontae, "Circular dichroism glucose biosensor based on chiral cadmium sulfide quantum dots," Sens. Actuators, B **274**, 402–411 (2018).
44. C. Carrillo-Carrion, S. Cardenas, B. M. Simonet, and M. Valcarcel, "Selective quantification of carnitine enantiomers using chiral cysteine-capped CdSe(ZnS) quantum dots," Anal. Chem. **81**(12), 4730–4733 (2009).
45. L. Song, S. Wang, N. A. Kotov, and Y. Xia, "Nonexclusive fluorescent sensing for L/D enantiomers enabled by dynamic nanoparticle-nanorod assemblies," Anal. Chem. **84**(17), 7330–7335 (2012).
46. R. Elghanian, J. J. Storhoff, R. C. Mucic, R. L. Letsinger, and C. A. Mirkin, "Selective colorimetric detection of polynucleotides based on the distance-dependent optical properties of gold nanoparticles," Science **277**(5329), 1078–1081 (1997).
47. D. G. Thompson, A. Enright, K. Faulds, W. E. Smith, and D. Graham, "Ultrasensitive DNA detection using oligonucleotide-silver nanoparticle conjugates," Anal. Chem. **80**(8), 2805–2810 (2008).
48. W. Zhao, W. Chiuman, J. C. Lam, S. A. McManus, W. Chen, Y. Cui, R. Pelton, M. A. Brook, and Y. Li, "DNA aptamer folding on gold nanoparticles: from colloid chemistry to biosensors," J. Am. Chem. Soc. **130**(11), 3610–3618 (2008).
49. J. Wang, L. Wang, X. Liu, Z. Liang, S. Song, W. Li, G. Li, and C. Fan, "A Gold Nanoparticle-Based Aptamer Target Binding Readout for ATP Assay," Adv. Mater. **19**, 3943–3946 (2007).
50. P. M. Tessier, J. Jinkoji, Y. C. Cheng, J. L. Prentice, and A. M. Lenhoff, "Self-interaction nanoparticle spectroscopy: a nanoparticle-based protein interaction assay," J. Am. Chem. Soc. **130**(10), 3106–3112 (2008).
51. M. Scampicchio, A. Arecchi, and S. Mannino, "Optical nanoprobes based on gold nanoparticles for sugar sensing," Nanotechnology 20(2009).
52. J. Liu and Y. Lu, "A colorimetric lead biosensor using DNAzyme-directed assembly of gold nanoparticles," J. Am. Chem. Soc. **125**(22), 6642–6643 (2003).
53. C. Yy, "Colorimetric assay for lead ions based on the leaching of gold nanoparticles," Anal. Chem. **81**(22), 9433–9439 (2009).
54. Y. Wang, X. Zhou, C. Xu, Y. Jin, and B. Li, "Gold Nanorods as Visual Sensing Platform for Chiral Recognition with Naked Eyes," Sci Rep **8**(1), 5296 (2018).
55. G. Song, C. Xu, and B. Li, "Visual chiral recognition of mandelic acid enantiomers with l-tartaric acid-capped gold nanoparticles as colorimetric probes," Sens. Actuators, B **215**, 504–509 (2015).
56. M. Zhang and B.-C. Ye, "Colorimetric Chiral Recognition of Enantiomers Using the Nucleotide-Capped Silver Nanoparticles," Anal. Chem. **83**(5), 1504–1509 (2011).
57. M. Kobayashi, S. Tomita, K. Sawada, K. Shiba, H. Yanagi, I. Yamashita, and Y. Uraoka, "Chiral meta-molecules consisting of gold nanoparticles and genetically engineered tobacco mosaic virus," Opt. Express **20**(22), 24856–24863 (2012).
58. C. Sachse, J. Z. Chen, P. D. Coureux, M. E. Stroupe, M. Fandrich, and N. Grigorieff, "High-resolution electron microscopy of helical specimens: a fresh look at tobacco mosaic virus," J Mol Biol **371**(3), 812–835 (2007).
59. A. O. Govorov, "Plasmon-Induced Circular Dichroism of a Chiral Molecule in the Vicinity of Metal Nanocrystals. Application to Various Geometries," J. Phys. Chem. C **115**(16), 7914–7923 (2011).
60. M. L. Nesterov, X. Yin, M. Schäferling, H. Giessen, and T. Weiss, "The Role of Plasmon-Generated Near Fields for Enhanced Circular Dichroism Spectroscopy," ACS Photonics **3**(4), 578–583 (2016).
61. X. Yin, M. Schaferling, B. Metzger, and H. Giessen, "Interpreting chiral nanophotonic spectra: the plasmonic Born-Kuhn model," Nano Lett. **13**(12), 6238–6243 (2013).

62. M. E. Layani, A. Ben Moshe, M. Varenik, O. Regev, H. Zhang, A. O. Govorov, and G. Markovich, "Chiroptical Activity in Silver Cholate Nanostructures Induced by the Formation of Nanoparticle Assemblies," J. Phys. Chem. C **117**(43), 22240–22244 (2013).
63. L. Xu, Z. Xu, W. Ma, L. Liu, L. Wang, H. Kuang, and C. Xu, "Highly selective recognition and ultrasensitive quantification of enantiomers," J. Mater. Chem. B **1**(35), 4478–4483 (2013).
64. S. Wang and C. Chan, "Lateral optical force on chiral particles near a surface," Nat. Commun. **5**(1), 3307 (2014).
65. Z. Zhu, W. Liu, Z. Li, B. Han, Y. Zhou, Y. Gao, and Z. Tang, "Manipulation of collective optical activity in one-dimensional plasmonic assembly," ACS Nano **6**(3), 2326–2332 (2012).
66. F. Zhu, X. Li, Y. Li, M. Yan, and S. Liu, "Enantioselective Circular Dichroism Sensing of Cysteine and Glutathione with Gold Nanorods," Anal. Chem. **87**(1), 357–361 (2015).
67. Z. Xu, L. Xu, Y. Zhu, W. Ma, H. Kuang, L. Wang, and C. Xu, "Chirality based sensor for bisphenol A detection," Chemical Communications 48(2012).
68. Z. Xu, L. Xu, L. M. Liz-Marzán, W. Ma, N. A. Kotov, L. Wang, H. Kuang, and C. Xu, "Sensitive Detection of Silver Ions Based on Chiroplasmonic Assemblies of Nanoparticles," Adv. Opt. Mater. **1**, 626–630 (2013).
69. X. Zhao, X. Wu, L. Xu, W. Ma, H. Kuang, L. Wang, and C. Xu, "Building heterogeneous core–satellite chiral assemblies for ultrasensitive toxin detection," Biosens. Bioelectron. **66**, 554–558 (2015).
70. Y. Zhao, L. Xu, W. Ma, L. Wang, H. Kuang, C. Xu, and N. A. Kotov, "Shell-Engineered Chiroplasmonic Assemblies of Nanoparticles for Zeptomolar DNA Detection," Nano Lett. **14**(7), 3908–3913 (2014).
71. Y. Liu, M. Wei, L. Zhang, Y. Zhang, W. Wei, L. Yin, Y. Pu, and S. Liu, "Chiroplasmonic Assemblies of Gold Nanoparticles for Ultrasensitive Detection of 8-Hydroxy-2′-deoxyguanosine in Human Serum Sample," Anal. Chem. **88**(12), 6509–6514 (2016).
72. K. Claborn, E. Puklin-Faucher, M. Kurimoto, W. Kaminsky, and B. Kahr, "Circular dichroism imaging microscopy: application to enantiomorphous twinning in biaxial crystals of 1,8-dihydroxyanthraquinone," J. Am. Chem. Soc. **125**(48), 14825–14831 (2003).
73. M. F. Maestre and J. E. Katz, "A circular dichroism microspectrophotometer," Biopolymers **21**, 1899–1908 (1982).
74. Y. Shindo, M. Nishio, and S. Maeda, "Problems of CD spectrometers (V): Can we measure CD and LD simultaneously? Comments on differential polarization microscopy (CD and linear dichroism)," Biopolymers **30**, 405–413 (1990).
75. M. Savoini, X. Wu, M. Celebrano, J. Ziegler, P. Biagioni, S. C. Meskers, L. Duo, B. Hecht, and M. Finazzi, "Circular dichroism probed by two-photon fluorescence microscopy in enantiopure chiral polyfluorene thin films," J. Am. Chem. Soc. **134**(13), 5832–5835 (2012).
76. J. Hudecova, J. Kapitan, V. Baumruk, R. P. Hammer, T. A. Keiderling, and P. Bour, "Side chain and flexibility contributions to the Raman optical activity spectra of a model cyclic hexapeptide," J. Phys. Chem. A **114**(28), 7642–7651 (2010).
77. C. Mensch, R. Pendrill, G. Widmalm, and C. Johannessen, "Studying the glycan moiety of RNase B by means of Raman and Raman optical activity," Chemphyschem **15**, 2252–2254 (2014).
78. C. Johannessen, R. Pendrill, G. Widmalm, L. Hecht, and L. D. Barron, "Glycan structure of a high-mannose glycoprotein from Raman optical activity," Angew. Chem. Int. Ed. **50**(23), 5349–5351 (2011).
79. E. Van de Vondel, C. Mensch, and C. Johannessen, "Direct Measurements of the Crowding Effect in Proteins by Means of Raman Optical Activity," J. Phys. Chem. B **120**(5), 886–890 (2016).
80. L. D. Barron, L. Hecht, E. W. Blanch, and A. F. Bell, "Solution structure and dynamics of biomolecules from Raman optical activity," Prog. Biophys. Mol. Biol. **73**(1), 1–49 (2000).
81. M. Sun, Z. Zhang, P. Wang, Q. Li, F. Ma, and H. Xu, "Remotely excited Raman optical activity using chiral plasmon propagation in Ag nanowires," Light: Sci. Appl. **2**(11), e112 (2013).
82. L. D. Barron and A. D. Buckingham, "Rayleigh and Raman scattering from optically active molecules," Mol. Phys. **20**(6), 1111–1119 (1971).
83. J. R. Rouxel, Y. Zhang, and S. Mukamel, "X-ray Raman optical activity of chiral molecules," Chem. Sci. **10**(3), 898–908 (2019).
84. J.-B. Biot, "Phénomènes de polarisation successive, observés dans des fluides homogènes," Bull. Soc. Philomath **190**, 1815 (1815).
85. S. Yoo and Q. H. Park, "Metamaterials and chiral sensing: a review of fundamentals and applications," Nanophotonics **8**(2), 249–261 (2019).
86. S. Chandrasekhar, "Optical rotatory dispersion of crystals," Proc. R. Soc. Lond. A **259**(1299), 531–553 (1961).
87. F. Egidi, I. Carnimeo, and C. Cappelli, "Optical rotatory dispersion of methyloxirane in aqueous solution: assessing the performance of density functional theory in combination with a fully polarizable QM/MM/PCM approach," Optical Materials Express 5(2014).
88. N. Hagen and T. Tadokoro, "The rainbow beam experiment: direct visualization of dipole scattering and optical rotatory dispersion," Proc Spie 11132(2019).
89. C. Stark, C. A. Carvajal Arrieta, R. Behroozian, B. Redmer, F. Fiedler, and S. Muller, "Broadband polarimetric glucose determination in protein containing media using characteristic optical rotatory dispersion," Biomed. Opt. Express **10**(12), 6340–6350 (2019).
90. T. J. Ward and D.-M. Hamburg, "Chiral separations," Anal. Chem. **76**(16), 4635–4644 (2004).

91. Y. Tang and A. E. Cohen, "Enhanced enantioselectivity in excitation of chiral molecules by superchiral light," Science **332**(6027), 333–336 (2011).
92. N. V. Vitanov and M. Drewsen, "Highly efficient detection and separation of chiral molecules through shortcuts to adiabaticity," Phys. Rev. Lett. **122**(17), 173202 (2019).
93. D. S. Bradshaw and D. L. Andrews, "Laser optical separation of chiral molecules," Opt. Lett. **40**(4), 677–680 (2015).
94. D. S. Bradshaw and D. L. Andrews, "Chiral discrimination in optical trapping and manipulation," New J. Phys. **16**(10), 103021 (2014).
95. R. P. Cameron, S. M. Barnett, and A. M. Yao, "Discriminatory optical force for chiral molecules," New J. Phys. **16**(1), 013020 (2014).
96. K. Y. Bliokh, A. Y. Bekshaev, and F. Nori, "Extraordinary momentum and spin in evanescent waves," Nat. Commun. **5**(1), 3300 (2014).
97. A. Hayat, J. B. Mueller, and F. Capasso, "Lateral chirality-sorting optical forces," Proc. Natl. Acad. Sci. **112**(43), 13190–13194 (2015).
98. M. Alizadeh and B. R. M. Reinhard, "Transverse chiral optical forces by chiral surface plasmon polaritons," ACS Photonics **2**(12), 1780–1788 (2015).
99. A. A. Saleh and J. A. Dionne, "Toward efficient optical trapping of sub-10-nm particles with coaxial plasmonic apertures," Nano Lett. **12**(11), 5581–5586 (2012).
100. G. Cipparrone, A. Mazzulla, A. Pane, R. J. Hernandez, and R. Bartolino, "Chiral Materials: Chiral Self-Assembled Solid Microspheres: A Novel Multifunctional Microphotonic Device (Adv. Mater. 48/2011)," Adv. Mater. **23**, 5704 (2011).
101. R. J. Hernández, A. Mazzulla, A. Pane, K. Volke-Sepúlveda, and G. Cipparrone, "Attractive-repulsive dynamics on light-responsive chiral microparticles induced by polarized tweezers," Lab Chip **13**(3), 459–467 (2013).
102. M. Donato, J. Hernandez, A. Mazzulla, C. Provenzano, R. Saija, R. Sayed, S. Vasi, A. Magazzù, P. Pagliusi, and R. Bartolino, "Polarization-dependent optomechanics mediated by chiral microresonators," Nat. Commun. **5**(1), 3656 (2014).
103. N. Kravets, A. Aleksanyan, H. Chraïbi, J. Leng, and E. Brasselet, "Optical enantioseparation of racemic emulsions of chiral microparticles," Phys. Rev. Appl. **11**(4), 044025 (2019).
104. G. Tkachenko and E. Brasselet, "Optofluidic sorting of material chirality by chiral light," Nat. Commun. **5**(1), 3577 (2014).
105. G. Tkachenko and E. Brasselet, "Spin controlled optical radiation pressure," Phys. Rev. Lett. **111**(3), 033605 (2013).
106. G. Tkachenko and E. Brasselet, "Helicity-dependent three-dimensional optical trapping of chiral microparticles," Nat. Commun. **5**(1), 4491 (2014).
107. N. Kravets, A. Aleksanyan, and E. Brasselet, "Chiral optical Stern-Gerlach newtonian experiment," Phys. Rev. Lett. **122**(2), 024301 (2019).
108. R. P. Cameron, S. M. Barnett, and A. M. Yao, "Optical helicity of interfering waves," J. Mod. Opt. **61**(1), 25–31 (2014).
109. A. Ivinskaya, M. I. Petrov, A. A. Bogdanov, I. Shishkin, P. Ginzburg, and A. S. Shalin, "Plasmon-assisted optical trapping and anti-trapping," Light: Sci. Appl. **6**(5), e16258 (2017).
110. Y. Pang and R. Gordon, "Optical trapping of a single protein," Nano Lett. **12**(1), 402–406 (2012).
111. A. Grigorenko, N. Roberts, M. Dickinson, and Y. Zhang, "Nanometric optical tweezers based on nanostructured substrates," Nat. Photonics **2**(6), 365–370 (2008).
112. M. Righini, P. Ghenuche, S. Cherukulappurath, V. Myroshnychenko, F. J. García de Abajo, and R. Quidant, "Nano-optical trapping of Rayleigh particles and Escherichia coli bacteria with resonant optical antennas," Nano Lett. **9**(10), 3387–3391 (2009).
113. W. Zhang, L. Huang, C. Santschi, and O. J. Martin, "Trapping and sensing 10 nm metal nanoparticles using plasmonic dipole antennas," Nano Lett. **10**(3), 1006–1011 (2010).
114. D. Yoo, K. L. Gurunatha, H.-K. Choi, D. A. Mohr, C. T. Ertsgaard, R. Gordon, and S.-H. Oh, "Low-power optical trapping of nanoparticles and proteins with resonant coaxial nanoaperture using 10 nm gap," Nano Lett. **18**(6), 3637–3642 (2018).
115. J. Chen, Z. Kang, S. K. Kong, and H.-P. Ho, "Plasmonic random nanostructures on fiber tip for trapping live cells and colloidal particles," Opt. Lett. **40**(17), 3926–3929 (2015).
116. A. A. Al Balushi and R. Gordon, "Label-free free-solution single-molecule protein–small molecule interaction observed by double-nanohole plasmonic trapping," ACS Photonics **1**(5), 389–393 (2014).
117. A. Kotnala and R. Gordon, "Double nanohole optical tweezers visualize protein p53 suppressing unzipping of single DNA-hairpins," Biomed. Opt. Express **5**(6), 1886–1894 (2014).
118. A. A. Al Balushi and R. Gordon, "A label-free untethered approach to single-molecule protein binding kinetics," Nano Lett. **14**(10), 5787–5791 (2014).
119. Z. Xu, W. Song, and K. B. Crozier, "Direct particle tracking observation and Brownian dynamics simulations of a single nanoparticle optically trapped by a plasmonic nanoaperture," ACS Photonics **5**(7), 2850–2859 (2018).
120. Y. Zhao, A. A. Saleh, M. A. Van De Haar, B. Baum, J. A. Briggs, A. Lay, O. A. Reyes-Becerra, and J. A. Dionne, "Nanoscopic control and quantification of enantioselective optical forces," Nat. Nanotechnol. **12**(11), 1055–1059 (2017).

121. Y. Liu and X. Zhang, "Metamaterials: a new frontier of science and technology," Chem. Soc. Rev. **40**(5), 2494–2507 (2011).
122. C. Zhou, X. Duan, and N. Liu, "A plasmonic nanorod that walks on DNA origami," Nat. Commun. **6**(1), 8102 (2015).
123. X. Lan, X. Lu, C. Shen, Y. Ke, W. Ni, and Q. Wang, "Au nanorod helical superstructures with designed chirality," J. Am. Chem. Soc. **137**(1), 457–462 (2015).
124. E. S. P. Leong, J. Deng, E. H. Khoo, S. Wu, W. K. Phua, and Y. J. Liu, "Fabrication of suspended, three-dimensional chiral plasmonic nanostructures with single-step electron-beam lithography," RSC Adv. **5**(117), 96366–96371 (2015).
125. M. Rajaei, J. Zeng, M. Albooyeh, M. Kamandi, M. Hanifeh, F. Capolino, and H. K. Wickramasinghe, "Giant circular dichroism at visible frequencies enabled by plasmonic ramp-shaped nanostructures," ACS Photonics **6**(4), 924–931 (2019).
126. A. Radke, T. Gissibl, T. Klotzbücher, P. V. Braun, and H. Giessen, "Three-dimensional bichiral plasmonic crystals fabricated by direct laser writing and electroless silver plating," Adv. Mater. **23**, 3018–3021 (2011).
127. N. Jiang, "On the spatial resolution limit of direct-write electron beam lithography," Microelectron. Eng. **168**, 41–44 (2017).
128. M. J. Urban, P. K. Dutta, P. Wang, X. Duan, X. Shen, B. Ding, Y. Ke, and N. Liu, "Plasmonic Toroidal Metamolecules Assembled by DNA Origami," J. Am. Chem. Soc. **138**(17), 5495–5498 (2016).
129. C. Song, M. G. Blaber, G. Zhao, P. Zhang, H. C. Fry, G. C. Schatz, and N. L. Rosi, "Tailorable plasmonic circular dichroism properties of helical nanoparticle superstructures," Nano Lett. **13**(7), 3256–3261 (2013).
130. C. Zhou, X. Duan, and N. Liu, "DNA-Nanotechnology-Enabled Chiral Plasmonics: From Static to Dynamic," Acc. Chem. Res. **50**(12), 2906–2914 (2017).
131. M. Wang, J. Dong, C. Zhou, H. Xie, W. Ni, S. Wang, H. Jin, and Q. Wang, "Reconfigurable Plasmonic Diastereomers Assembled by DNA Origami," ACS Nano **13**(12), 13702–13708 (2019).
132. A. Kuzyk, Y. Yang, X. Duan, S. Stoll, A. O. Govorov, H. Sugiyama, M. Endo, and N. Liu, "A light-driven three-dimensional plasmonic nanosystem that translates molecular motion into reversible chiroptical function," Nat. Commun. **7**(1), 10591 (2016).
133. N. C. Seeman, "Nucleic acid junctions and lattices," J. Theor. Biol. **99**(2), 237–247 (1982).
134. R. Jungmann, S. Renner, and F. C. Simmel, "From DNA nanotechnology to synthetic biology," HFSP J. **2**(2), 99–109 (2008).
135. A. Kuzuya and M. Komiyama, "Design and construction of a box-shaped 3D-DNA origami," Chem Commun (Camb), 4182–4184 (2009).
136. J. J. Funke, P. Ketterer, C. Lieleg, S. Schunter, P. Korber, and H. Dietz, "Uncovering the forces between nucleosomes using DNA origami," Sci Adv. **2**(11), e1600974 (2016).
137. N. V. Voigt, T. Torring, A. Rotaru, M. F. Jacobsen, J. B. Ravnsbaek, R. Subramani, W. Mamdouh, J. Kjems, A. Mokhir, F. Besenbacher, and K. V. Gothelf, "Single-molecule chemical reactions on DNA origami," Nat. Nanotechnol. **5**(3), 200–203 (2010).
138. S. Pal, Z. Deng, B. Ding, H. Yan, and Y. Liu, "DNA-origami-directed self-assembly of discrete silver-nanoparticle architectures," Angew Chem Int Ed Engl **49**(15), 2700–2704 (2010).
139. W. P. Klein, R. P. Thomsen, K. B. Turner, S. A. Walper, J. Vranish, J. Kjems, M. G. Ancona, and I. L. Medintz, "Enhanced catalysis from multienzyme cascades assembled on a DNA origami triangle," ACS Nano **13**(12), 13677–13689 (2019).
140. Q. Zhang, Q. Jiang, N. Li, L. Dai, Q. Liu, L. Song, J. Wang, Y. Li, J. Tian, and B. Ding, "DNA origami as an in vivo drug delivery vehicle for cancer therapy," ACS Nano **8**(7), 6633–6643 (2014).
141. J. N. Anker, W. P. Hall, O. Lyandres, N. C. Shah, J. Zhao, and R. P. Van Duyne, "Biosensing with plasmonic nanosensors," Nat. Mater. **7**(6), 442–453 (2008).
142. E. Winfree, F. Liu, L. A. Wenzler, and N. C. Seeman, "Design and self-assembly of two-dimensional DNA crystals," Nature **394**(6693), 539–544 (1998).
143. F. Mathieu, S. Liao, J. Kopatsch, T. Wang, C. Mao, and N. C. Seeman, "Six-helix bundles designed from DNA," Nano Lett. **5**(4), 661–665 (2005).
144. A. Chworos, I. Severcan, A. Y. Koyfman, P. Weinkam, E. Oroudjev, H. G. Hansma, and L. Jaeger, "Building programmable jigsaw puzzles with RNA," Science **306**(5704), 2068–2072 (2004).
145. P. Yin, R. F. Hariadi, S. Sahu, H. M. Choi, S. H. Park, T. H. LaBean, and J. H. Reif, "Programming DNA tube circumferences," Science **321**(5890), 824–826 (2008).
146. D. Liu, S. H. Park, J. H. Reif, and T. H. LaBean, "DNA nanotubes self-assembled from triple-crossover tiles as templates for conductive nanowires," Proc. Natl. Acad. Sci. **101**(3), 717–722 (2004).
147. D. Han, S. Pal, J. Nangreave, Z. Deng, Y. Liu, and H. Yan, "DNA origami with complex curvatures in three-dimensional space," Science **332**(6027), 342–346 (2011).
148. R. P. Goodman, I. A. Schaap, C. F. Tardin, C. M. Erben, R. M. Berry, C. F. Schmidt, and A. J. Turberfield, "Rapid chiral assembly of rigid DNA building blocks for molecular nanofabrication," Science **310**(5754), 1661–1665 (2005).
149. S. Pal, Z. Deng, H. Wang, S. Zou, Y. Liu, and H. Yan, "DNA directed self-assembly of anisotropic plasmonic nanostructures," J. Am. Chem. Soc. **133**(44), 17606–17609 (2011).

150. R. Chhabra, J. Sharma, Y. Ke, Y. Liu, S. Rinker, S. Lindsay, and H. Yan, “Spatially addressable multiprotein nanoarrays templated by aptamer-tagged DNA nanoarchitectures,” J. Am. Chem. Soc. **129**(34), 10304–10305 (2007).
151. J. Sharma, R. Chhabra, C. S. Andersen, K. V. Gothelf, H. Yan, and Y. Liu, “Toward reliable gold nanoparticle patterning on self-assembled DNA nanoscaffold,” J. Am. Chem. Soc. **130**(25), 7820–7821 (2008).
152. F. Hong, F. Zhang, Y. Liu, and H. Yan, “DNA Origami: Scaffolds for Creating Higher Order Structures,” Chem. Rev. **117**(20), 12584–12640 (2017).
153. H. Bui, C. Onodera, C. Kidwell, Y. Tan, E. Graugnard, W. Kuang, J. Lee, W. B. Knowlton, B. Yurke, and W. L. Hughes, “Programmable periodicity of quantum dot arrays with DNA origami nanotubes,” Nano Lett. **10**(9), 3367–3372 (2010).
154. H. T. Maune, S. P. Han, R. D. Barish, M. Bockrath, W. A. Goddard III, W. P. Rothemund, and E. Winfree, “Self-assembly of carbon nanotubes into two-dimensional geometries using DNA origami templates,” Nat. Nanotechnol. **5**(1), 61–66 (2010).
155. N. Stephanopoulos, M. Liu, G. J. Tong, Z. Li, Y. Liu, H. Yan, and M. B. Francis, “Immobilization and one-dimensional arrangement of virus capsids with nanoscale precision using DNA origami,” Nano Lett. **10**(7), 2714–2720 (2010).
156. K. Lund, A. J. Manzo, N. Dabby, N. Michelotti, A. Johnson-Buck, J. Nangreave, S. Taylor, R. Pei, M. N. Stojanovic, N. G. Walter, E. Winfree, and H. Yan, “Molecular robots guided by prescriptive landscapes,” Nature **465**(7295), 206–210 (2010).
157. X. Shen, P. Zhan, A. Kuzyk, Q. Liu, A. Asenjo-Garcia, H. Zhang, F. J. de Abajo, A. Govorov, B. Ding, and N. Liu, “3D plasmonic chiral colloids,” Nanoscale **6**(4), 2077–2081 (2014).
158. Z. Fan and A. O. Govorov, “Chiral nanocrystals: plasmonic spectra and circular dichroism,” Nano Lett. **12**(6), 3283–3289 (2012).
159. M. J. Urban, C. Zhou, X. Duan, and N. Liu, “Optically Resolving the Dynamic Walking of a Plasmonic Walker Couple,” Nano Lett. **15**(12), 8392–8396 (2015).
160. E. M. Roller, L. K. Khorashad, M. Fedoruk, R. Schreiber, A. O. Govorov, and T. Liedl, “DNA-assembled nanoparticle rings exhibit electric and magnetic resonances at visible frequencies,” Nano Lett. **15**(2), 1368–1373 (2015).
161. A. J. Thubagere, W. Li, R. F. Johnson, Z. Chen, S. Doroudi, Y. L. Lee, G. Izatt, S. Wittman, N. Srinivas, D. Woods, E. Winfree, and L. Qian, “A cargo-sorting DNA robot,” Science 357(2017).
162. Y. Huang, M. K. Nguyen, A. K. Natarajan, V. H. Nguyen, and A. Kuzyk, “A DNA Origami-Based Chiral Plasmonic Sensing Device,” ACS Appl. Mater. Interfaces **10**(51), 44221–44225 (2018).
163. D. Y. Zhang and G. Seelig, “Dynamic DNA nanotechnology using strand-displacement reactions,” Nat. Chem. **3**(2), 103–113 (2011).
164. Y. Dong, Z. Yang, and D. Liu, “DNA nanotechnology based on i-motif structures,” Acc. Chem. Res. **47**(6), 1853–1860 (2014).
165. T. Gerling, K. F. Wagenbauer, A. M. Neuner, and H. Dietz, “Dynamic DNA devices and assemblies formed by shape-complementary, non-base pairing 3D components,” Science **347**(6229), 1446–1452 (2015).
166. Y. Kamiya and H. Asanuma, “Light-driven DNA nanomachine with a photoresponsive molecular engine,” Acc. Chem. Res. **47**(6), 1663–1672 (2014).
167. Y. B. Zheng, Y. W. Yang, L. Jensen, L. Fang, B. K. Juluri, A. H. Flood, P. S. Weiss, J. F. Stoddart, and T. J. Huang, “Active molecular plasmonics: controlling plasmon resonances with molecular switches,” Nano Lett. **9**(2), 819–825 (2009).
168. S. Zhang, J. Zhou, Y. S. Park, J. Rho, R. Singh, S. Nam, A. K. Azad, H. T. Chen, X. Yin, A. J. Taylor, and X. Zhang, “Photoinduced handedness switching in terahertz chiral metamolecules,” Nat. Commun. **3**(1), 942 (2012).
169. A. Kuzyk, R. Schreiber, H. Zhang, A. O. Govorov, T. Liedl, and N. Liu, “Reconfigurable 3D plasmonic metamolecules,” Nat. Mater. **13**(9), 862–866 (2014).
170. M. K. Nguyen and A. Kuzyk, “Reconfigurable Chiral Plasmonics beyond Single Chiral Centers,” ACS Nano **13**(12), 13615–13619 (2019).
171. M. Hentschel, M. Schaferling, B. Metzger, and H. Giessen, “Plasmonic diastereomers: adding up chiral centers,” Nano Lett. **13**(2), 600–606 (2013).
172. A. Kuzyk, M. J. Urban, A. Idili, F. Ricci, and N. Liu, “Selective control of reconfigurable chiral plasmonic metamolecules,” Sci Adv. **3**(4), e1602803 (2017).
173. R. D. Vale, “The molecular motor toolbox for intracellular transport,” Cell **112**(4), 467–480 (2003).
174. N. Liu, M. Hentschel, T. Weiss, A. P. Alivisatos, and H. Giessen, “Three-dimensional plasmon rulers,” Science **332**(6036), 1407–1410 (2011).
175. X. Zhang, F. Fan, Y. Y. Ji, and S. J. Chang, “Temperature-dependent chirality of cholesteric liquid crystal for terahertz waves,” Opt. Lett. **45**(18), 4988–4991 (2020).
176. X. Shen, C. Song, J. Wang, D. Shi, Z. Wang, N. Liu, and B. Ding, “Rolling up gold nanoparticle-dressed DNA origami into three-dimensional plasmonic chiral nanostructures,” J. Am. Chem. Soc. **134**(1), 146–149 (2012).
177. A. Kuzyk, R. Schreiber, Z. Fan, G. Pardatscher, E. M. Roller, A. Hogele, F. C. Simmel, A. O. Govorov, and T. Liedl, “DNA-based self-assembly of chiral plasmonic nanostructures with tailored optical response,” Nature **483**(7389), 311–314 (2012).
178. M. V. Gorkunov, O. Y. Rogov, A. V. Kondratov, V. V. Artemov, R. V. Gainutdinov, and A. A. Ezhov, “Chiral visible light metasurface patterned in monocrystalline silicon by focused ion beam,” Sci. Rep. **8**(1), 11623 (2018).

179. I. Sakellari, X. Yin, M. L. Nesterov, K. Terzaki, A. Xomalis, and M. Farsari, “3D chiral plasmonic metamaterials fabricated by direct laser writing: the twisted omega particle,” Adv. Opt. Mater. **5**, 1700200 (2017).
180. B. Frank, X. Yin, M. Schäferling, J. Zhao, S. M. Hein, P. V. Braun, and H. Giessen, “Large-area 3D chiral plasmonic structures,” ACS Nano **7**(7), 6321–6329 (2013).
181. A. Veroli, B. Alam, L. Maiolo, F. Todisco, L. Dominici, M. De Giorgi, G. Pettinari, A. Gerardino, and A. Benedetti, “Planar chiral plasmonic 2D metamaterial: design and fabrication,” in *AIP Conference Proceedings*, (AIP Publishing LLC, 2019), 020015.
182. H.-B. Sun, T. Tanaka, and S. Kawata, “Three-dimensional focal spots related to two-photon excitation,” Appl. Phys. Lett. **80**(20), 3673–3675 (2002).
183. M. Thiel, H. Fischer, G. von Freymann, and M. Wegener, “Three-dimensional chiral photonic superlattices,” Opt. Lett. **35**(2), 166–168 (2010).
184. J. C. W. Lee and C. Chan, “Polarization gaps in spiral photonic crystals,” Opt. Express **13**(20), 8083–8088 (2005).
185. J. K. Gansel, M. Latzel, A. Frölich, J. Kaschke, M. Thiel, and M. Wegener, “Tapered gold-helix metamaterials as improved circular polarizers,” Appl. Phys. Lett. **100**(10), 101109 (2012).
186. M. Esposito, V. Tasco, F. Todisco, A. Benedetti, D. Sanvitto, and A. Passaseo, “Three dimensional chiral metamaterial nanospirals in the visible range by vertically compensated focused ion beam induced-deposition,” Adv. Opt. Mater. **2**(2), 154–161 (2014).
187. M. Esposito, V. Tasco, F. Todisco, M. Cuscunà, A. Benedetti, D. Sanvitto, and A. Passaseo, “Triple-helical nanowires by tomographic rotatory growth for chiral photonics,” Nat. Commun. **6**(1), 6484 (2015).
188. Z. Wang, Y. Wang, G. Adamo, J. Teng, and H. Sun, “Induced optical chirality and circularly polarized emission from achiral CdSe/ZnS quantum dots via resonantly coupling with plasmonic chiral metasurfaces,” Laser Photonics Rev. **13**, 1800276 (2019).
189. V. Tasco, M. Esposito, F. Todisco, A. Benedetti, M. Cuscunà, D. Sanvitto, and A. Passaseo, “Three-dimensional nanohelices for chiral photonics,” Appl. Phys. A **122**(4), 280 (2016).
190. Y. Chen, J. Gao, and X. Yang, “Chiral metamaterials of plasmonic slanted nanoapertures with symmetry breaking,” Nano Lett. **18**(1), 520–527 (2018).
191. M. Hentschel, M. Schaferling, T. Weiss, N. Liu, and H. Giessen, “Three-dimensional chiral plasmonic oligomers,” Nano Lett. **12**(5), 2542–2547 (2012).
192. Y. Qu, Y. Bai, T. Aba, H. Ullah, A. Abudukelimu, J. Huang, T. Gou, J. Li, and Z. Zhang, “Chiral Near-Fields Induced by Plasmonic Chiral Conic Nanoshell Metallic Nanostructure for Sensitive Biomolecule Detection,” J. Phys. Chem. C **124**(25), 13912–13919 (2020).
193. M. Manoccio, M. Esposito, E. Primiceri, A. Leo, C. Massimo, T. Vittorianna, D. Zuev, Y. Sun, G. Maruccio, and G. Gigli, “Femtomolar Biodetection by a Compact Core-Shell 3D Chiral Metamaterial,” arXiv preprint arXiv:2102.02107 (2021).
194. D. Simeone, M. Esposito, M. Scuderi, G. Calafiore, G. Palermo, A. De Luca, F. Todisco, D. Sanvitto, G. Nicotra, and S. Cabrini, “Tailoring electromagnetic hot spots toward visible frequencies in ultra-narrow gap Al/Al2O3 bowtie nanoantennas,” ACS Photonics **5**(8), 3399–3407 (2018).
195. B. L. Feringa, R. A. van Delden, N. Koumura, and E. M. Geertsema, “Chiroptical molecular switches,” Chem. Rev. **100**(5), 1789–1816 (2000).
196. R. Arnell, N. Ferraz, and T. Fornstedt, “Analytical Characterization of Chiral Drug– Protein Interactions: Comparison between the Optical Biosensor (Surface Plasmon Resonance) Assay and the HPLC Perturbation Method,” Anal. Chem. **78**(5), 1682–1689 (2006).